J. Fluid Mech. (2013), *vol.* 726, *pp.* 596–623.
doi:10.1017/jfm.2013.249

Koopman-mode decomposition of the cylinder wake

Shervin Bagheri†

Linné Flow Centre, Department of Mechanics KTH, SE-10044 Stockholm, Sweden

(Received 22 August 2012; revised 1 February 2013; accepted 13 May 2013;
first published online 11 June 2013)

The Koopman operator provides a powerful way of analysing nonlinear flow dynamics using linear techniques. The operator defines how observables evolve in time along a nonlinear flow trajectory. In this paper, we perform a Koopman analysis of the first Hopf bifurcation of the flow past a circular cylinder. First, we decompose the flow into a sequence of Koopman modes, where each mode evolves in time with one single frequency/growth rate and amplitude/phase, corresponding to the complex eigenvalues and eigenfunctions of the Koopman operator, respectively. The analytical construction of these modes shows how the amplitudes and phases of nonlinear global modes oscillating with the vortex shedding frequency or its harmonics evolve as the flow develops and later sustains self-excited oscillations. Second, we compute the dynamic modes using the dynamic mode decomposition (DMD) algorithm, which fits a linear combination of exponential terms to a sequence of snapshots spaced equally in time. It is shown that under certain conditions the DMD algorithm approximates Koopman modes, and hence provides a viable method to decompose the flow into saturated and transient oscillatory modes. Finally, the relevance of the analysis to frequency selection, global modes and shift modes is discussed.

Key words: instability, nonlinear dynamical systems, vortex shedding

1. Introduction

Flows in ducts, corners, cavities and past bluff bodies belong to a category of fluid systems where self-sustained oscillations emerge from stationary conditions as a control parameter is varied. It is of great practical significance to identify emerging and saturated coherent structures associated with self-excited frequencies in the flow, since they often lead to large structural vibrations, acoustic noise and resonance. The objective of this paper is to represent the fluid flow as the superposition of global flow structures, called Koopman modes (Mezić 2005, 2013), whose discrete frequencies and growth rates are integer multiples of one another. Compared to standard harmonic analysis, the present approach provides, in addition to saturated modes, growing/decaying structures that may exists during a transient phase, i.e. when the flow is not fully saturated. The identification of the modes and their associated frequencies/growth rates can be formulated as an eigenvalue (or spectral) problem of the Koopman operator (Koopman 1931). This linear operator is not related to the

† Email address for correspondence: shervin@mech.kth.se

linearized Navier–Stokes operator, which is often employed in local stability analyses. Instead it provides an indirect description of the full nonlinear flow through the linear dynamics of observable functions of the state (such as kinetic energy, probe signals etc.). It may seem surprising that there exists a linear description of inherently nonlinear phenomena, but there is a caveat; namely, that the spectrum of the Koopman operator may become arbitrarily difficult to analyse, involving continuous, degenerate eigenvalues corresponding to eigenfunctions that are non-smooth and singular. In this paper, we consider a flow approaching and evolving on a limit cycle. For this particular nonlinear problem, the Koopman spectrum is discrete and the eigenfunctions are regular. They may also be directly related to commonly known concepts developed for flows with self-sustained oscillations, such as global modes (Huerre & Monkewitz 1990), mean flows and shift modes (Noack *et al.* 2003).

One algorithm that is able to extract oscillatory modes with growth rates from a sequence of nonlinear flow samples is dynamic mode decomposition (DMD) introduced by Schmid (2010). The so-called dynamic modes produced by DMD, have received a great deal of attention (Schmid *et al.* 2011; Schmid 2011; Seena & Sung 2011; Chen, Tu & Rowley 2012; Duke, Soria & Honnery 2012; Muld, Efraimsson & Henningson 2012; Semeraro, Bellani & Lundell 2012), partially because the algorithm is computationally cheap and can be applied to huge data sets. The connection between dynamic modes and Koopman modes was first made in Rowley *et al.* (2009). This work showed that an expansion of the flow field into dynamic modes and Koopman modes is in the same (spectral) form, but whereas the former expansion is finite and the latter is infinite.

The present study is motivated by further clarifying the connection between Koopman modes and dynamic modes as well as their physical significance for flows with distinct self-sustained oscillations. We focus on the configuration of the flow past a circular cylinder in the Reynolds number range where only one limit cycle exists. We analytically derive the Koopman modes and compare them to the computational modes provided by the DMD algorithm. Prior to Mezić (2005), essentially all the applied literature has focused on the adjoint Koopman operator: the well-known Perron–Frobenious operator. Since an adjoint operator has the same spectrum as its direct counterpart, the majority of the analysis of the present paper is related to the theory developed for the Perron–Frobenious operator (Lasota & Mackey 1994; Gaspard 1998; Cvitanović *et al.* 2013). In particular, the efficient computation of the Perron–Frobenius eigenvalues is based on forming the trace of the linear operator (Cvitanović & Eckhardt 1991). It is precisely the formula derived in Cvitanović & Eckhardt (1991) for the Perron–Frobenious operator that we will use to find the analytical form of Koopman eigenvalues.

There exists a number of alternative techniques for extracting oscillatory modes from a fluid system. As already mentioned, one of them is a harmonic analysis, for example a temporal discrete Fourier transform of sampled data. This approach estimates a set of oscillating modes, but the decomposition requires a predetermined set of frequencies and periodic sampled data. For more complex flows it can be a cumbersome (and risky) task to estimate global fundamental frequencies from local probe signals, before extracting global oscillating modes. A local procedure for estimating global frequencies has been developed in the classical global mode approach (Huerre & Monkewitz 1990). The theory, which is valid for parallel or weakly non-parallel flows, established that the existence of a sufficiently large region of local absolute instability implies that the entire flow can sustain self-sustained oscillations. Based on this theory, local analyses of most of the canonical parallel

or weakly non-parallel flows have been conducted in order to predict the vortex shedding frequency. An alternative approach (see e.g. Pier 2002; Barkley 2006; Thiria & Wesfreid 2007 and references therein) to identify coherent structures that can be associated with vortex shedding is based on a linear analysis of the time-averaged mean flow. For the cylinder wake, this technique provides global modes whose discrete frequencies are in good agreement with the harmonics of the vortex shedding frequency (Barkley 2006). However, such an analysis is not guaranteed to work for other configurations (Sipp & Lebedev 2007) and to some extent lacks a theoretical foundation. Finally, the use of the proper orthogonal decomposition (POD) (Lumley 1970) should be mentioned in this context. The method ranks coherent structures based on their energy content by diagonalizing the time-averaged spatial correlation tensor. Pairs of POD modes may correspond to oscillating flow structures if the flow (thus the kinetic energy) is strongly dominated by periodic vortex shedding, but since the method averages in time, there is no guarantee that it can pin down one structure to one frequency. It was realized by Noack *et al.* (2003) that if the POD basis is augmented by an additional 'shift' mode representing a mean flow modification, the extended basis can accurately capture the transient dynamics. As demonstrated by the present study, the current approach naturally takes into account transient flow regimes by providing modes which in addition to a frequency also have a growth/decay rate.

The paper is organized as follows. Section 2 describes the essential dynamics of the cylinder wake and the associated numerical method. The section ends with defining a spectral expansion of the flow. In § 3, we briefly present the standard weakly nonlinear analysis, which results in the one-dimensional Stuart–Landau (S–L) equation. Section 4 introduces the linear Koopman operator with respect to the S–L equation and derives the associated eigenvalues and eigenfunctions. Moreover, the Koopman modes of the cylinder wake at Reynolds number, Re, near the critical threshold for vortex shedding are derived. The leading modes are categorized and their physical significance is discussed. Section 5 presents numerical results for the flow past a circular cylinder at $Re = 50$. The dynamic modes and values extracted from the DMD algorithm are compared to the Koopman modes and eigenvalues presented in § 4. In § 6, the Koopman eigenvalues at Reynolds number significantly above the critical one are derived using a well-known trace formula from periodic-orbit theory (Cvitanović *et al.* 2013).

2. Flow dynamics near onset of bifurcation

2.1. *Configuration and discretization*

We consider an infinitely long circular cylinder of diameter D in a uniform flow U_∞. The fluid motion is governed by the two-dimensional incompressible Navier–Stokes (N–S) equations,

$$\frac{\partial \boldsymbol{u}}{\partial t} = -\boldsymbol{u}\cdot\boldsymbol{\nabla}\boldsymbol{u} + \frac{1}{Re}\Delta\boldsymbol{u} - \boldsymbol{\nabla}p + \boldsymbol{F}_b, \tag{2.1a}$$

$$0 = \boldsymbol{\nabla}\cdot\boldsymbol{u}, \tag{2.1b}$$

where $\boldsymbol{u}(\boldsymbol{x},t) = \boldsymbol{u}(x,y,t)$ is the velocity field and $p(\boldsymbol{x},t)$ and $\boldsymbol{F}_b(\boldsymbol{x},t)$ are Lagrange multipliers to enforce, respectively, fluid incompressibility and boundary conditions. The Reynolds number is defined as $Re = U_\infty D/\nu$ where ν is the viscosity.

Equations (2.1) are discretized with a staggered-grid finite-volume (second-order) fractional step formulation (Perot 1993) using a second-order semi-implicit time

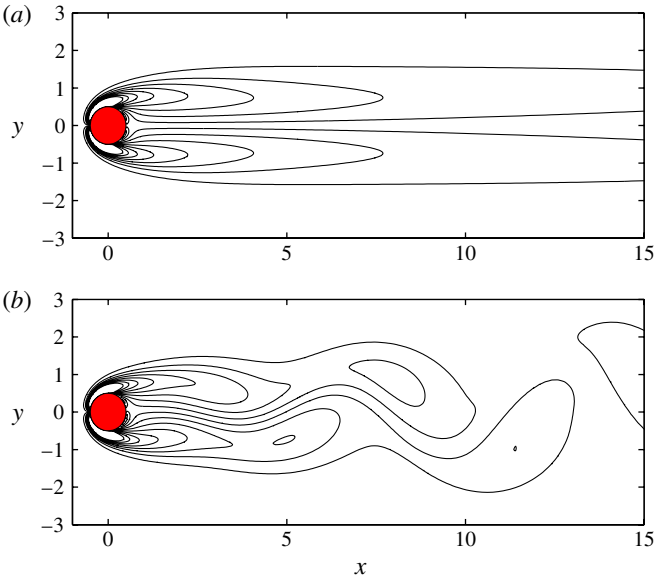

FIGURE 1. (Colour online) Flow past a circular cylinder at $Re = 50$. The contours depict the vorticity field (levels are set from -3 to 3 with increments of 0.4) of the unstable equilibrium solution (a) and of a snapshot of the time-periodic solution (b).

integration. The computational grid does not conform to the cylinder. Instead the no-slip boundary condition is enforced at Lagrangian points defining the cylinder boundary by appropriate regularized surface forces $\boldsymbol{F}_b$ (Taira & Colonius 2007). We use a domain that is $L_x = 60D$ long and $L_y = 40D$ wide with a resolution of $N_x = 450$ and $N_y = 300$ in the longitudinal and transverse directions, respectively. The grid is non-uniform, with the minimum grid spacing $h = 1/30$ near the cylinder boundary. We impose a uniform inflow $(U_\infty, 0)$, convective outflow and symmetric boundary conditions on the lateral domain sides. The solver has been validated by benchmarking the lift and drag coefficients for various Reynolds numbers with those found in the literature. Henceforth, both the flow field in (2.1) and its spatially discretized counterpart of dimension $n = 2N_xN_y$ will be denoted by $\boldsymbol{u}(t)$; a distinction between them will be made explicitly if it is necessary.

For Reynolds number below the critical value of $Re_c = 46.6$, the flow consists of two steady symmetrical vortices. At $Re = Re_c$ the wake begins to oscillate periodically, shedding alternating vortices from the upper and lower lateral sides of the cylinder. As shown by Provansal, Mathis & Boyer (1987), this corresponds to a Hopf bifurcation, i.e. the system (2.1) develops self-sustained oscillations (a limit cycle) from a stable stationary flow (an equilibrium). Thus, for $Re > Re_c$, the flow system has two critical elements co-existing: an attracting limit cycle and an unstable equilibrium. In figure 1(a) the unstable equilibrium is shown at $Re = 50$. It was obtained by following the stable branch from $Re = 40$ into the supercritical regime. When the steady solution is perturbed by a small localized asymmetric perturbation, the unstable eigenmode of the stability matrix grows exponentially and after a transient time it saturates on the limit cycle. An instantaneous flow field on the limit cycle at $Re = 50$ is shown in figure 1(b).

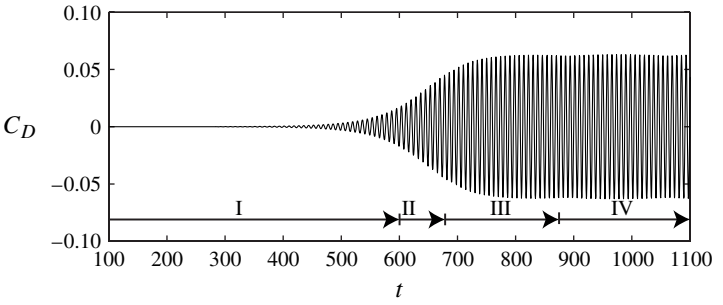

FIGURE 2. The drag coefficient C_D as a function of time for the flow past a circular cylinder at $Re = 50$. Intervals I–III pertain to transient dynamics, whereas interval IV pertains to the saturated limit cycle dynamics.

2.2. *Problem formulation*

The general objective is to find a representation of the flow field in the form

$$\boldsymbol{u}(t) = \sum_{j=0}^{\infty} \phi_j \boldsymbol{v}_j \exp[(\sigma_j + \mathrm{i}\omega_j)t], \tag{2.2}$$

where $\phi_j \in \mathbb{C}$ is the amplitude, and $\boldsymbol{v}_j$ a complex-valued flow structure associated with the growth rate σ_j and the frequency ω_j. For reasons that will become clear in the following sections, we refer to amplitudes ϕ_j as Koopman eigenfunctions, the flow structures $\boldsymbol{v}_j$ as Koopman modes and $\lambda_j = \sigma_j + \mathrm{i}\omega_j$ as Koopman eigenvalues of the Navier–Stokes equations.

To characterize the saturation onto a limit cycle of a flow starting near the unstable equilibrium, the evolution of the non-dimensional horizontal (drag) force on the cylinder C_D is shown in figure 2. One can identify four time scales associated with the time intervals marked I–IV in the figure: I, exponential escape rate from the unstable equilibrium; II, algebraic growth due to the interaction of the equilibrium and the limit cycle; III, exponential relaxation rate to the limit cycle; and IV, period of the oscillations on the limit cycle. Let us anticipate how a flow with these four time scales may described by the expansion (2.2). First, if a term in the modal expansion basis is unstable ($\sigma_j > 0$), then as $t \to \infty$, it will dominate compared to the stable terms and an unbounded behaviour is predicted. However, the flow is bounded in time since it settles on the limit cycle. As a consequence, there cannot be any asymptotically growing structures and thus $\sigma_j \leqslant 0$ for all modes in (2.2). Second, the algebraic time scale (interval II) is non-modal (Schmid 2007) and cannot be captured by individual exponential terms. The intervals I and II can be treated by introducing a generalization (Gaspard *et al.* 1995; Gaspard & Tasaki 2001) of (2.2) and will reported in a future investigation. The remainder of this paper deals with Koopman terms pertaining to the attracting (interval III) and asymptotic (interval IV) dynamics. In particular, if $\sigma_j \neq 0$ then $\boldsymbol{v}_j$ is a transient Koopman mode in the local stable manifold (i.e. defined as all states that approach the limit cycle exponentially fast, see Guckenheimer & Holmes 1983) of the limit cycle, whereas modes with $\sigma_j = 0$ capture asymptotic dynamics on the limit cycle.

In the next section, we define amplitude functions governed by the S–L equation, by separating the time scales associated with saturation (slow) and oscillation (fast). Then

in § 4, functions of the amplitude (referred to as observables) will be expanded in the eigenfunctions of the Koopman operator in order to construct the expansion (2.2).

3. Multiple-scale expansion of the flow field

Close to the critical Reynolds number, the time (τ) it takes for the state starting near the unstable equilibrium to saturate on the limit cycle is long compared to the characteristic time scale of the flow, i.e. the limit cycle period, $t_p = 2\pi/\omega$. A multiple-scale analysis can be performed by separating the dynamics associated with the scales τ and t. This will determine an amplitude equation (Chomaz 2005) that describes the nonlinear transient dynamics in the vicinity of the bifurcation point. This section summarizes the 'global' multiple-scale approach presented in Sipp & Lebedev (2007), where the reader can find more details.

Consider a Reynolds number slightly larger than the critical value for the onset of oscillations,

$$1/Re = 1/Re_c - \epsilon, \quad 0 < \epsilon \ll 1. \tag{3.1}$$

Introduce a long time scale $\tau = \epsilon t$ and expand the flow field as

$$\boldsymbol{u}(t) = \boldsymbol{u}_s + \epsilon^{1/2}\boldsymbol{u}_1(\tau, t) + \epsilon\boldsymbol{u}_2(\tau, t) + \epsilon^{3/2}\boldsymbol{u}_3(\tau, t) + \cdots \tag{3.2}$$

where $\boldsymbol{u}_s$ is the steady equilibrium point of the Navier–Stokes equation. Inserting (3.2) and (3.1) into (2.1), one obtains a sequence of equations at orders $\sqrt{\epsilon}^k$ for $k = 0, 1, 2 \ldots$. The zeroth-order equation is the steady Navier–Stokes equation for $\boldsymbol{u}_s$,

$$-(\boldsymbol{u}_s \cdot \boldsymbol{\nabla})\boldsymbol{u}_s + \frac{1}{Re_c}\nabla^2\boldsymbol{u}_s - \boldsymbol{\nabla}p_0 = 0,$$

where p_0 is chosen such that $\boldsymbol{\nabla} \cdot \boldsymbol{u}_s = 0$. This equation is satisfied by construction, since $\boldsymbol{u}_s$ is an equilibrium.

3.1. *Order* $\sqrt{\epsilon}^1$

The leading-order ($\sqrt{\epsilon}^1$) equation is

$$\frac{\partial \boldsymbol{u}_1}{\partial t} = \boldsymbol{A}\boldsymbol{u}_1, \tag{3.3}$$

where $\boldsymbol{A}$ represents the linearized equation around $\boldsymbol{u}_s$ at the critical Reynolds number i.e.

$$\boldsymbol{A}\boldsymbol{u}_1 = -(\boldsymbol{u}_s \cdot \boldsymbol{\nabla})\boldsymbol{u}_1 - (\boldsymbol{u}_1 \cdot \boldsymbol{\nabla})\boldsymbol{u}_s + \frac{1}{Re_c}\nabla^2\boldsymbol{u}_1 - \boldsymbol{\nabla}p_1.$$

The multiplier p_1 is chosen such that $\boldsymbol{u}_1$ is incompressible. For $Re = Re_c$, the spectrum of $\boldsymbol{A}$ is restricted to the stable half-plane with two neutral eigenvalues on the imaginary axis. The neutral eigenfunction $\tilde{\boldsymbol{u}}_1$ of $\boldsymbol{A}$ with zero growth rate and frequency ω_0 satisfies

$$\boldsymbol{A}\tilde{\boldsymbol{u}}_1 = \mathrm{i}\omega_0\tilde{\boldsymbol{u}}_1, \tag{3.4}$$

and governs the long-term dynamics. We may thus let

$$\boldsymbol{u}_1(\tau, t) = A(\tau)\mathrm{e}^{\mathrm{i}\omega_0 t}\tilde{\boldsymbol{u}}_1 + \text{c.c.}, \tag{3.5}$$

where $A(\tau)$ is a complex scalar amplitude evolving on a slow time scale and c.c. denotes the complex conjugate. This expansion term is called the first harmonic.

3.2. *Order* $\sqrt{\epsilon}^2$

The second-order term satisfies a linear equation as in (3.3), but now it is inhomogeneous,

$$\frac{\partial \boldsymbol{u}_2}{\partial t} = \boldsymbol{A}\boldsymbol{u}_2 + \boldsymbol{F}_2^{(1)} + |A|^2\boldsymbol{F}_2^{(2)} + (A^2\mathrm{e}^{2\mathrm{i}\omega_0 t}\boldsymbol{F}_2^{(3)} + \text{c.c.}), \tag{3.6}$$

where

$$\boldsymbol{F}_2^{(1)} = -\nabla^2\boldsymbol{u}_s, \tag{3.7a}$$

$$\boldsymbol{F}_2^{(2)} = -\tilde{\boldsymbol{u}}_1\cdot\nabla\tilde{\boldsymbol{u}}_1^* - \tilde{\boldsymbol{u}}_1^*\cdot\nabla\tilde{\boldsymbol{u}}_1, \tag{3.7b}$$

$$\boldsymbol{F}_2^{(3)} = \nabla\tilde{\boldsymbol{u}}_1\cdot\nabla\tilde{\boldsymbol{u}}_1. \tag{3.7c}$$

For $A = 0$ only the steady forcing term $\boldsymbol{F}_2^{(1)}$ is present. It represents the modification of the neutral equilibrium $\boldsymbol{u}_s$ at $1/Re_c$ to an unstable equilibrium at $1/Re_c - \epsilon$. Thus, physically, the destabilization at leading order is caused by a negative diffusion term. Due to the quadratic nonlinear term in the N–S equation, we have two forcing terms arising from the first harmonic $\boldsymbol{u}_1$: $|A|^2\boldsymbol{F}_2^{(2)}$ varies on slow time scale τ and describes the interaction of $\boldsymbol{u}_1$ with its complex conjugate; $A^2\mathrm{e}^{2\mathrm{i}\omega_0 t}\boldsymbol{F}_2^{(3)}$ varies on both time scales (τ and t) and describes the interaction of $\boldsymbol{u}_1$ with itself.

Since (3.6) is linear, we may write the solution as the superposition of $\tilde{\boldsymbol{u}}_2^{(1)}, \tilde{\boldsymbol{u}}_2^{(2)}$ and $\tilde{\boldsymbol{u}}_2^{(3)}$ corresponding to the response of the linear system to $\boldsymbol{F}_2^{(1)}, \boldsymbol{F}_2^{(2)}$ and $\boldsymbol{F}_2^{(3)}$, respectively, i.e.

$$\boldsymbol{u}_2 = \tilde{\boldsymbol{u}}_2^{(1)} + |A^2|\tilde{\boldsymbol{u}}_2^{(2)} + (A^2\mathrm{e}^{2\mathrm{i}\omega_0 t}\tilde{\boldsymbol{u}}_2^{(3)} + \text{c.c.}), \tag{3.8}$$

where

$$\tilde{\boldsymbol{u}}_2^{(1)} = -\boldsymbol{A}^{-1}\boldsymbol{F}_2^{(1)}, \quad \tilde{\boldsymbol{u}}_2^{(2)} = -\boldsymbol{A}^{-1}\boldsymbol{F}_2^{(2)} \quad \text{and} \quad \tilde{\boldsymbol{u}}_2^{(3)} = -(\mathrm{i}2\omega_0\boldsymbol{I} - \boldsymbol{A})^{-1}\boldsymbol{F}_2^{(3)}. \tag{3.9}$$

We call $\tilde{\boldsymbol{u}}_2^{(1)}$, $\tilde{\boldsymbol{u}}_2^{(2)}$ and $\tilde{\boldsymbol{u}}_2^{(3)}$, the basic flow modification, the zeroth harmonic and the second harmonic, respectively.

3.3. *Order* $\sqrt{\epsilon}^3$

The third-order equation with forcing terms proportional to $\exp(\mathrm{i}\omega_0 t)$ is

$$\frac{\partial \boldsymbol{u}_3}{\partial t} = \boldsymbol{A}\boldsymbol{u}_3 + \exp(\mathrm{i}\omega_0 t)\left(-\frac{\partial A}{\partial \tau}\boldsymbol{u}_1 + A\boldsymbol{F}_3^{(1)} + |A|^2A\boldsymbol{F}_3^{(2)} + \text{c.c.}\right) + \cdots, \tag{3.10}$$

where

$$\boldsymbol{F}_3^{(1)} = -\nabla\tilde{\boldsymbol{u}}_1\cdot\nabla\tilde{\boldsymbol{u}}_2^{(1)} - \tilde{\boldsymbol{u}}_2^{(1)}\cdot\nabla\tilde{\boldsymbol{u}}_1 - \nabla^2\tilde{\boldsymbol{u}}_1, \tag{3.11a}$$

$$\boldsymbol{F}_3^{(2)} = -\nabla\tilde{\boldsymbol{u}}_1\cdot\nabla\tilde{\boldsymbol{u}}_2^{(2)} - \tilde{\boldsymbol{u}}_2^{(2)}\cdot\nabla\tilde{\boldsymbol{u}}_1 - \nabla\tilde{\boldsymbol{u}}_1^*\cdot\nabla\tilde{\boldsymbol{u}}_2^{(3)} - \tilde{\boldsymbol{u}}_2^{(3)}\cdot\nabla\tilde{\boldsymbol{u}}_1^*. \tag{3.11b}$$

The term $\boldsymbol{F}_3^{(1)}$ involves the interaction of the first harmonic with the basic flow modification as well as a negative diffusion of $\tilde{\boldsymbol{u}}_1$. The second forcing term $\boldsymbol{F}_3^{(2)}$ arises due to the interaction of the first harmonic with the zeroth and second harmonics.

In order to solve (3.10) for $\tilde{\boldsymbol{u}}_3$, one may assume that

$$\boldsymbol{u}_3 = A\mathrm{e}^{\mathrm{i}\omega_0 t}\tilde{\boldsymbol{u}}_3^{(1)} + |A|^2A\mathrm{e}^{\mathrm{i}\omega_0 t}\tilde{\boldsymbol{u}}_3^{(2)} + \text{c.c.} + \cdots. \tag{3.12}$$

However, each part of $\tilde{\boldsymbol{u}}_3^{(j)}$ is not a solution to the linear problem with the forcing term $\boldsymbol{F}_3^{(j)}$, since $\mathrm{i}\omega_0$ is an eigenvalue of $\boldsymbol{A}$ and thus $(\mathrm{i}\omega_0\boldsymbol{I} + \boldsymbol{A})^{-1}$ is not invertible. To find a

unique solution, we choose

$$\frac{\partial A}{\partial \tau} = a_0 A - a_1 A|A|^2, \tag{3.13}$$

and thus include additional constraints involving the complex scalars a_0 and a_1. This compatibility condition is the Stuart–Landau equation, governing the complex amplitude A on a slow time scale τ. The scalar parameters of the S–L equation can be determined by forming the inner product with the left eigenfunction of $\boldsymbol{A}$ (see e.g. Sipp & Lebedev 2007).

Using (3.5), (3.8) and (3.12) and rearranging the terms according to their behaviour in t, we can write the expansion (3.2) as

$$\begin{aligned}\boldsymbol{u}(t) = \boldsymbol{u}_s &+ \epsilon(\tilde{\boldsymbol{u}}_2^{(1)} + |A|^2\tilde{\boldsymbol{u}}_2^{(2)}) + \cdots \\ &+ A(\tau)\mathrm{e}^{\mathrm{i}\omega_0 t}(\sqrt{\epsilon}\tilde{\boldsymbol{u}}_1 + \epsilon^{3/2}\tilde{\boldsymbol{u}}_3^{(1)} + \epsilon^{3/2}|A|^2\tilde{\boldsymbol{u}}_3^{(2)} + \cdots) \\ &+ A(\tau)^2\mathrm{e}^{2\mathrm{i}\omega_0 t}(\epsilon\tilde{\boldsymbol{u}}_2^{(3)} + \cdots) + \text{c.c.} + \cdots.\end{aligned} \tag{3.14}$$

In the next section we take the final step in the construction of (2.2) by expressing the temporal modulations of the amplitudes appearing in (3.14) in exponential form.

4. Koopman analysis

In the subsequent analysis, it is convenient to work with the S–L equation (3.13) in polar coordinates $A(\tau) = r(\tau)\exp(\mathrm{i}\theta(\tau))$,

$$\frac{\partial r}{\partial \tau} = f_1(r) = \mu r - r^3, \tag{4.1a}$$

$$\frac{\partial \theta}{\partial \tau} = f_2(r) = \gamma - \beta r^2, \tag{4.1b}$$

where $a_0 = \mu + \mathrm{i}\gamma$ and $a_1 = 1 + \mathrm{i}\beta$. Given the initial condition $A_0 = r_0\mathrm{e}^{\mathrm{i}\theta_0}$, the solution of (4.1) at a later time $\tau > 0$ is given by

$$r(\tau) = r_0\left(\frac{\mu}{r_0^2 + (\mu - r_0^2)\exp(-2\mu\tau)}\right)^{1/2}, \tag{4.2a}$$

$$\theta(\tau) = \theta_0 + \omega_1\tau + \beta\ln\left(\frac{r(\tau)}{r_0}\right), \tag{4.2b}$$

where $\omega_1 = \gamma - \mu\beta$. An analysis of (4.2) shows that the amplitude approaches the attracting limit cycle at $r = \sqrt{\mu}$ exponentially fast with the Lyapunov exponent -2μ and then oscillates with the frequency ω_1.

The amplitudes $A, A^2, |A|^2$ and $|A|^2A$ in (3.14) may be regarded as scalar-valued observables $g(A) : \mathbb{C} \to \mathbb{C}$ of the S–L equation. Note that g depends implicitly on τ. The time evolution of $g(A)$ is governed by the differential operator (Lasota & Mackey 1994) $L = (\boldsymbol{f}\cdot\nabla)$, where $\boldsymbol{f} = (f_1, f_2)$, i.e.

$$\frac{\partial g}{\partial \tau} = \left(f_1(r)\frac{\partial}{\partial r} + f_2(r)\frac{\partial}{\partial \theta}\right)g = Lg. \tag{4.3}$$

This system is linear and infinite-dimensional. Note however that the observable can be a nonlinear function of A. We define the evolution operator of (4.3),

$$U_\tau = \exp(L\tau), \tag{4.4}$$

as the *Koopman operator* (Koopman 1931; Lasota & Mackey 1994). This operator provides a linear description, which is also valid far from equilibrium points, without the explicit linearization of (4.1). Note that (4.1) and (4.2) predict the nonlinear motion of the amplitude A. The pair of equations (4.3) and (4.4), on the other hand, characterize the transport of any (possibly nonlinear) function of the amplitude $g(A)$.

4.1. *Spectrum of the Koopman operator*

One objective of this paper is to use the spectral properties of U_τ to characterize the flow as it approaches and settles on the limit cycle. To this end, we define the observables $\phi_j : \mathbb{C} \to \mathbb{C}$ and the complex scalars $\hat{\lambda}_j \in \mathbb{C}$ that satisfy

$$L\phi_j(A) = \hat{\lambda}_j \phi_j(A), \quad j = 0, 1, 2, \ldots, \tag{4.5}$$

as the Koopman eigenfunctions and Koopman eigenvalues of the S–L equation, respectively. We must choose a particular category of observable functions in order to determine $\hat{\lambda}_j$. This is because the spectrum of L depends on the choice of space of functions that the Koopman operator is acting on. In this paper the functions $g(A)$ are assumed to be real-analytical functions, i.e. functions for which the Taylor expansion is convergent at each point A. This choice of smooth and bounded observables simplifies the mathematical treatment of the spectrum significantly (Artuso, Hugh & Cvitanović 2013). In particular, the spectrum becomes discrete as in (4.5).

In polar coordinates, $\phi_j(re^{i\theta})$ is a periodic function of the phase θ, and may thus be expressed as a Fourier series,

$$\phi_j = \sum_{m=-\infty}^{\infty} \hat{\phi}_{j,m}(r) \exp(im\theta), \tag{4.6}$$

where $\hat{\phi}_{j,m}(r)$ denotes the Fourier coefficient. Inserting this expansion into (4.5) one obtains

$$L\phi_{j,m}(A) = \hat{\lambda}_{j,m} \phi_{j,m}(A), \tag{4.7}$$

for $j = 0, 1, 2, \ldots$, $m = 0, \pm 1, \pm 2, \ldots$ and $\phi_{j,m} = \hat{\phi}_{j,m}(r) \exp(im\theta)$. Since L in (4.3) is not self-adjoint, the Koopman eigenfunctions $\phi_{j,m}$ are not mutually orthogonal functions. The eigenfunctions are bi-orthogonal to a set of functions $\psi_{i,n}$, i.e.

$$\langle \phi_{j,m}, \psi_{i,n} \rangle = \delta_{ij}\delta_{nm}. \tag{4.8}$$

Assume that $g(A) \in \mathrm{span}(\phi_{j,m})$, then using the bi-orthogonality condition, $g(A)$ can be expanded as

$$g(A) = \sum_{j=0}^{\infty} \sum_{m=-\infty}^{\infty} \alpha_{j,m}^{(g)} \phi_{j,m}(r) \exp(\hat{\lambda}_{j,m}\tau), \tag{4.9}$$

where the (j, m)th expansion coefficient in (4.9) is given by

$$\alpha_{j,m}^{(g)} = \langle \psi_{j,m}, g(A) \rangle. \tag{4.10}$$

By considering the flow evolving only in intervals III and IV in figure 2, we can find an analytical spectrum of L with respect to the S–L equation. Note that restricting the dynamics to the local stable manifold and to the limit cycle does not mean that the derived Koopman eigenvalues are local and valid only in these regions. It can be shown using the trace formula (see Cvitanović & Eckhardt 1991, and appendix B)

that for real-analytical observables the full discrete spectrum is simply the union of the eigenvalues associated with all the equilibria and periodic orbits that may exist in state space. Thus the spectrum of L is patched together by eigenvalues directly associated to different critical elements. We refer readers to Gaspard (1998) for details. In appendix A, we derive that for the limit cycle the expansion coefficients are given by

$$\alpha_{j,m}^{(g)} = \left\{ \frac{1}{j!} \frac{\partial^{(j)}}{\partial y} \left[\hat{g}_m \left(\sqrt{\frac{\mu}{1+y}} \right) (1+y)^{-\mathrm{i}m\beta/2} \right] \right\}_{y=0}, \tag{4.11}$$

where $\hat{g}_m$ is the Fourier coefficient of $g(A)$. From (4.11) one may evaluate any expansion coefficient of any analytical observable. For example for $g(A) = |A|^2$, the zeroth expansion coefficient is

$$\alpha_{0,0}^{(|A|^2)} = \left\{ \left(\frac{\mu}{1+y} \right) (1+y)^{-\mathrm{i}m\beta/2} \right\}_{y=0} = \mu. \tag{4.12}$$

The Koopman eigenfunctions and eigenvalues satisfying (4.7) (see appendix A) are

$$\phi_{j,m} = \left(\frac{\mu}{r_0^2} - 1 \right)^j \exp\left[\mathrm{i}m \left(\theta_0 + \beta \ln \left(\frac{\sqrt{\mu}}{r_0} \right) \right) \right], \tag{4.13}$$

and

$$\hat{\lambda}_{j,m} = -j2\mu + \mathrm{i}m\omega_1, \tag{4.14}$$

respectively. We observe from (4.13) that Koopman eigenfunctions are nonlinear functions of r_0. To demonstrate how nonlinearity is taken into account, consider the first three expansion terms of $g(A) = |A|^2$:

$$|A|^2 = \mu - \mu \left(\frac{\mu}{r_0^2} - 1 \right) \mathrm{e}^{-2\mu\tau} + \mu \left(\frac{\mu}{r_0^2} - 1 \right)^2 \mathrm{e}^{-4\mu\tau} + \cdots. \tag{4.15}$$

The nonlinear evolution of $|A|^2$ is thus described as a linear combination of a steady term and a sequence of exponentially decaying nonlinear functions of r_0.

4.2. *Spectral expansion of N–S equations*

The combination of the multiple-scale expansion of the flow field (3.14) and the spectral expansion of the observable amplitudes (4.9) yields the Koopman modes. In (3.14), the following amplitudes arise: $A, A^2, |A|^2$ and $A|A|^2$. Each of them can be expanded in Koopman eigenfunctions (4.13) of the S–L equation,

$$\begin{aligned} \boldsymbol{u}(t) = \boldsymbol{u}_s &+ \epsilon \tilde{\boldsymbol{u}}_2^{(1)} + \left(\sum_{j=0}^{\infty} \alpha_{j,0}^{(|A|^2)} \phi_{j,0} \mathrm{e}^{\hat{\lambda}_{j,0}\tau} \right) \epsilon \tilde{\boldsymbol{u}}_2^{(2)} \\ &+ \left(\sum_{j=0}^{\infty} \alpha_{j,1}^{(A)} \phi_{j,1} \mathrm{e}^{\hat{\lambda}_{j,1}\tau} \right) \mathrm{e}^{\mathrm{i}\omega_0 t} (\sqrt{\epsilon} \tilde{\boldsymbol{u}}_1 + \epsilon^{3/2} \tilde{\boldsymbol{u}}_3^{(1)}) \\ &+ \left(\sum_{j=0}^{\infty} \alpha_{j,1}^{(A|A|^2)} \phi_{j,1} \mathrm{e}^{\hat{\lambda}_{j,1}\tau} \right) \mathrm{e}^{\mathrm{i}\omega_0 t} \epsilon^{3/2} \tilde{\boldsymbol{u}}_3^{(2)} \\ &+ \left(\sum_{j=0}^{\infty} \alpha_{j,2}^{(A^2)} \phi_{j,2} \mathrm{e}^{\hat{\lambda}_{j,2}\tau} \right) \mathrm{e}^{\mathrm{i}2\omega_0 t} \epsilon \tilde{\boldsymbol{u}}_2^{(3)} + \cdots. \end{aligned} \tag{4.16}$$

Note that the spectral expansions consist of a single sum; since the relevant observables are integer powers of A, only one non-zero Fourier coefficient appears in each expansion, i.e. $m = 1$ for $A = 1$, $m = 2$ for A^2, $m = 0$ for $|A|^2$ and $m = 1$ for $|A|^2 A$. Moreover, using (4.14) and $\tau = \epsilon t$, we may write the temporal part of the above expansion terms as

$$\lambda_{j,m} = \hat{\lambda}_{j,m}\epsilon + \mathrm{i}m\omega_0 = -2j\mu\epsilon + \mathrm{i}m(\omega_1\epsilon + \omega_0). \tag{4.17}$$

These complex values are defined as the Koopman eigenvalues with respect to the N–S equations. The real part is a multiple of the Lyapunov exponent $\sigma = -2\mu\epsilon$, characterizing the relaxation onto the limit cycle on a slow time scale. The imaginary part is a multiple of the frequency $\omega = \omega_1\epsilon + \omega_0$ of the saturated oscillating flow. It is composed of the frequency of the linear eigenfunction (ω_0) and the modification arising due the nonlinear saturation ($\omega_1\epsilon$). As shown in figure 3 the Koopman eigenvalues form a lattice in the stable half of the complex plane, with a horizontal and vertical spacing corresponding to ω and σ respectively. The expansion (4.16) can now be written in a spectral form,

$$\begin{aligned}
\boldsymbol{u}(t) = &\left[\boldsymbol{u}_s + \epsilon\tilde{\boldsymbol{u}}_2^{(1)} + \epsilon\alpha_{0,0}^{(|A|^2)}\tilde{\boldsymbol{u}}_2^{(2)}\right] + \sum_{j=1}^{\infty}\phi_{j,0}\left[\alpha_{j,0}^{(|A|^2)}\epsilon\tilde{\boldsymbol{u}}_2^{(2)}\right]\mathrm{e}^{\lambda_{j,0}t} \\
&+ \sum_{j=0}^{\infty}\phi_{j,1}\left[\left(\alpha_{j,1}^{(A)}(\sqrt{\epsilon}\tilde{\boldsymbol{u}}_1 + \epsilon^{3/2}\tilde{\boldsymbol{u}}_3^{(1)}) + \alpha_{j,1}^{(A|A|^2)}\epsilon^{3/2}\tilde{\boldsymbol{u}}_3^{(2)}\right)\right]\mathrm{e}^{\lambda_{j,1}t} \\
&+ \sum_{j=0}^{\infty}\phi_{j,2}\left[\alpha_{j,2}^{(A^2)}\epsilon\tilde{\boldsymbol{u}}_2^{(3)}\right]\mathrm{e}^{\lambda_{j,2}t} + \cdots \\
= &\,\boldsymbol{v}_{0,0} + \sum_{j=1}^{\infty}\phi_{j,0}\boldsymbol{v}_{j,0}\mathrm{e}^{\lambda_{j,0}t} + \sum_{j=0}^{\infty}\phi_{j,1}\boldsymbol{v}_{j,1}\mathrm{e}^{\lambda_{j,1}t} + \sum_{j=0}^{\infty}\phi_{j,2}\boldsymbol{v}_{j,2}\mathrm{e}^{\lambda_{j,2}t} + \cdots,
\end{aligned} \tag{4.18}$$

where the Koopman modes $\boldsymbol{v}_{0,0}, \boldsymbol{v}_{j,0}, \boldsymbol{v}_{j,1}$ and $\boldsymbol{v}_{j,2}$ of (2.1) are defined as the terms in square brackets in the above equation. Note that the expansion of $g(A) = |A|^2$ which appears in the first line of (4.16) has been split into two parts. As observed from (4.15) the first expansion term of this observable has the Koopman eigenfunction $\phi_{0,0} = 1$ corresponding to the eigenvalue $\hat{\lambda}_{0,0} = 0$. This stationary term is proportional to $\tilde{\boldsymbol{u}}_2^{(2)}$ and is treated separately above. As stated in Rowley *et al.* (2009), we can regard the above expression (4.18) as expanding the flow field $\boldsymbol{u}(t)$ in a linear combination of the Koopman eigenfunction $\phi_{j,m}$, where the spatial structures $\boldsymbol{v}_{j,m}$ are the corresponding coefficients in the expansion. In our particular case, for which the Reynolds number is slightly above Re_c, the Koopman eigenfunctions $\phi_{j,m}$ are functions of the initial amplitude $A_0 = r_0\exp(\mathrm{i}\theta_0)$. As we have seen in § 3, for small ϵ the flow evolves in a slow manifold and the only degree of freedom is A. In the more general case when the Reynolds number is significantly larger than Re_c, there is no slow manifold and the Koopman eigenfunctions are functions of the full initial state $\boldsymbol{u}_0$.

The coefficients $\alpha_{j,m}^{(g)}$ may be calculated in a straightforward manner up to any order from (4.11). The leading-order expansion coefficients ($j = 0$, 1 and $m = 0$, 1, 2) are

$$\alpha_{0,1}^{(A)} = \sqrt{\mu}, \quad \alpha_{1,1}^{(A)} = -\sqrt{\mu}(1 + \mathrm{i}\beta)/2, \tag{4.19a}$$

$$\alpha_{0,2}^{(A^2)} = \mu, \quad \alpha_{1,2}^{(A^2)} = -\mu(1 + \mathrm{i}\beta), \tag{4.19b}$$

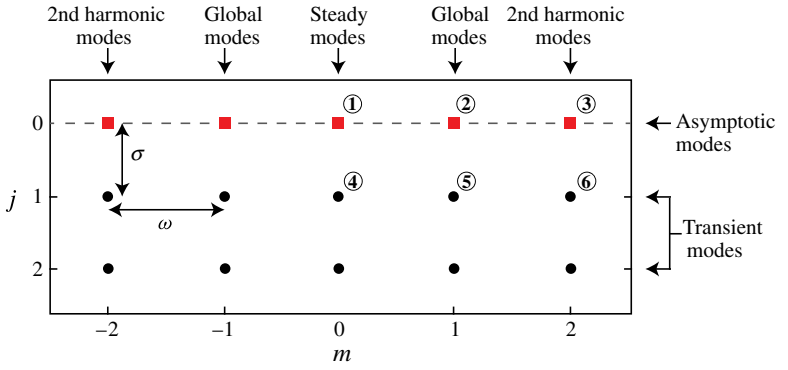

FIGURE 3. (Colour online) Koopman eigenvalues of the Navier–Stokes equation as given by the analytical expression (4.17). Squares (red online) and circles mark eigenvalues corresponding to the asymptotic and transient modes, respectively. Koopman modes associated with eigenvalues labelled ①–③ are given in (4.20)–(4.22), whereas ④–⑥ are given in (4.26)–(4.28).

$$\alpha_{0,0}^{(|A|^2)} = \mu, \quad \alpha_{1,0}^{(|A|^2)} = -\mu, \tag{4.19c}$$

$$\alpha_{0,1}^{(|A|^2A)} = \mu^{3/2}, \quad \alpha_{1,1}^{(|A|^2A)} = \mu^{3/2}(3 + \mathrm{i}\beta)/2. \tag{4.19d}$$

Inserting (4.19) into (4.18), the leading ($j = 0, 1$ and $m = 0, 1, 2$) Koopman modes are constructed explicitly up to order $\sqrt{\epsilon}^3$. We categorize the modes into two kinds: (i) asymptotic modes ($j = 0$), which describe the saturated dynamics on the limit cycle; (ii) the transient modes ($j \neq 0$), which evolve in the local stable manifold of the limit cycle.

4.3. *Asymptotic Koopman modes*

Three leading asymptotic Koopman modes ($j = 0, m = 1, 2, 3$) are

$$\boldsymbol{v}_{0,0} = \boldsymbol{u}_s + \epsilon\tilde{\boldsymbol{u}}_2^{(1)} + \epsilon\mu\tilde{\boldsymbol{u}}_2^{(2)}, \tag{4.20}$$

$$\boldsymbol{v}_{0,1} = \sqrt{\mu\epsilon}(\tilde{\boldsymbol{u}}_1 + \epsilon\tilde{\boldsymbol{u}}_3^{(1)} + \epsilon\mu\tilde{\boldsymbol{u}}_3^{(2)}), \tag{4.21}$$

$$\boldsymbol{v}_{0,2} = \epsilon\mu\tilde{\boldsymbol{u}}_2^{(3)}, \tag{4.22}$$

corresponding, respectively, to the following Koopman eigenvalues:

$$\lambda_{0,0} = 0, \quad \lambda_{0,1} = \mathrm{i}\omega, \quad \lambda_{0,2} = \mathrm{i}2\omega. \tag{4.23}$$

The eigenvalues are on the imaginary axis and integer multiples of the fundamental frequency of the limit cycle (square symbols in figure 3). Let us take closer look at the physical significance of the above Koopman modes. The first mode (4.20) corresponding to $\lambda_{0,0} = 0$ is the time-averaged mean flow. At the leading order, it is composed of $\boldsymbol{u}_s + \epsilon\tilde{\boldsymbol{u}}_2^{(1)}$, which is the unstable equilibrium at $Re = (1/Re_c - \epsilon)^{-1}$, and $\epsilon\tilde{\boldsymbol{u}}_2^{(2)}$, which arises due to the interaction of the first harmonic with its complex conjugate.

The asymptotic mode $\boldsymbol{v}_{0,1}$ in (4.21) corresponding to the eigenvalue $\lambda_{0,1} = \mathrm{i}\omega$, represents a structure oscillating with the fundamental frequency of the limit cycle (ω). It thus represent a global mode as defined by Huerre & Monkewitz (1990). The superposition of the first two terms $\sqrt{\epsilon}\tilde{\boldsymbol{u}}_1 + \epsilon^{3/2}\tilde{\boldsymbol{u}}_3^{(1)}$ is the unstable eigenfunction of the

linearized system around the equilibrium $\boldsymbol{u}_s + \epsilon\tilde{\boldsymbol{u}}_2^{(1)}$. The remaining term ($\epsilon^{3/2}\mu\tilde{\boldsymbol{u}}_3^{(2)}$) in $\boldsymbol{v}_{0,1}$ is the difference between the linear eigenfunction and the saturated fundamental mode of the limit cycle. It is generated due to the interaction of harmonics $\tilde{\boldsymbol{u}}_k$, $\tilde{\boldsymbol{u}}_l$ such that $k + l = 1$. The mode (4.22) represents an asymptotic structure oscillating with the second harmonic frequency of the limit cycle (2ω). This term arises due to the nonlinear interaction of the unstable eigenmode with itself.

The eigenfunctions corresponding to (4.20)–(4.22) are

$$|\phi_{0,0}| = 1, \quad \arg(\phi_{0,0}) = 0, \tag{4.24a}$$

$$|\phi_{0,1}| = 1, \quad \arg(\phi_{0,1}) = \theta_0 + \beta \ln\left(\frac{\sqrt{\mu}}{r_0}\right), \tag{4.24b}$$

$$|\phi_{0,2}| = 1, \quad \arg(\phi_{0,2}) = 2\theta_0 + 2\beta \ln\left(\frac{\sqrt{\mu}}{r_0}\right). \tag{4.24c}$$

The magnitude of the Koopman eigenfunctions of all asymptotic modes is one, whereas their phase depends on r_0. This is intuitive, since only the phase dynamics of the limit cycle should depend on the initial state. Assuming that the norms of the terms $\tilde{\boldsymbol{u}}_1, \tilde{\boldsymbol{u}}_2, \tilde{\boldsymbol{u}}_3$ appearing in (4.20)–(4.22) are of order one, we get the following scaling:

$$\|\boldsymbol{v}_{0,m}\|^2 \sim (\epsilon\mu)^{m/2}. \tag{4.25}$$

Since $\epsilon\mu < 1$, the norm of the asymptotic Koopman mode oscillating with m times the fundamental frequency decreases with the exponent $m/2$. As a consequence, Koopman modes with increasingly higher frequencies make a smaller contribution to the dynamics.

4.4. *Transient Koopman modes*

Three leading transient Koopman modes ($j = 1, m = 1, 2, 3$) are

$$\boldsymbol{v}_{1,0} = -\epsilon\mu\tilde{\boldsymbol{u}}_2^{(2)}, \tag{4.26}$$

$$\boldsymbol{v}_{1,1} = \frac{\sqrt{\mu\epsilon}}{2}\left((1 + \mathrm{i}\beta)(\tilde{\boldsymbol{u}}_1 + \epsilon\tilde{\boldsymbol{u}}_3^{(1)}) + \epsilon\mu(3 + \mathrm{i}\beta)\tilde{\boldsymbol{u}}_3^{(2)}\right), \tag{4.27}$$

$$\boldsymbol{v}_{1,2} = -\epsilon(1 + \mathrm{i}\beta)\mu\tilde{\boldsymbol{u}}_2^{(3)}, \tag{4.28}$$

corresponding, respectively, to the following Koopman eigenvalues:

$$\lambda_{1,0} = \sigma, \quad \lambda_{1,1} = \sigma + \mathrm{i}\omega, \quad \lambda_{1,2} = \sigma + \mathrm{i}2\omega. \tag{4.29}$$

These eigenvalues are aligned along a horizontal line at a distance $\sigma = -2\mu\epsilon$ from the imaginary axis (circle symbols in figure 3). The mode $\boldsymbol{v}_{1,0}$ in (4.26) is non-oscillatory and decaying with the Lyapunov exponent of the limit cycle (σ). Its spatial structure is proportional to the difference between the time-averaged flow ($\boldsymbol{v}_{0,0}$) and the steady unstable equilibrium ($\boldsymbol{u}_s + \epsilon\tilde{\boldsymbol{u}}_2^{(1)}$), i.e.

$$\boldsymbol{v}_{1,0} \sim \boldsymbol{v}_{0,0} - (\boldsymbol{u}_s + \epsilon\tilde{\boldsymbol{u}}_2^{(1)}). \tag{4.30}$$

In the applied model-reduction community such a structure is referred to as a 'shift mode'. Its importance for robustness in low-dimensional models has been demonstrated in many investigations (Noack *et al.* 2003; Tadmor *et al.* 2010).

The mode (4.27) oscillates with the fundamental frequency and decays with the Lyapunov exponent of the limit cycle. It has the same spatial ingredients as the

Mode	Eigenvalue	Name	Symmetry
$\boldsymbol{v}_{0,0}$	$\lambda_{0,0} = 0$	Mean flow	Symmetric
$\boldsymbol{v}_{1,0}$	$\lambda_{1,0} = \sigma$	Shift mode	Symmetric
$\boldsymbol{v}_{0,1}$	$\lambda_{0,1} = \mathrm{i}\omega$	Global mode	Antisymmetric
$\boldsymbol{v}_{1,1}$	$\lambda_{1,1} = \sigma + \mathrm{i}\omega$	Transient global mode	Antisymmetric
$\boldsymbol{v}_{0,2}$	$\lambda_{0,2} = \mathrm{i}2\omega$	2nd harmonic	Symmetric
$\boldsymbol{v}_{1,2}$	$\lambda_{1,2} = \sigma + \mathrm{i}2\omega$	Transient 2nd harmonic	Symmetric

TABLE 1. Properties of the leading Koopman modes of an oscillator. The symmetry of the modes is based on the assumption of a symmetric unstable equilibrium state $\boldsymbol{u}_s$.

asymptotic $\boldsymbol{v}_{0,1}$ in (4.21), but the relative contribution and phases of $\tilde{\boldsymbol{u}}_1, \tilde{\boldsymbol{u}}_3^{(1)}$ and $\tilde{\boldsymbol{u}}_3^{(2)}$ are different. This connection between the transient and asymptotic modes holds for all oscillatory structures, e.g. the transient higher harmonic Koopman mode (4.28) compared to (4.22) has the same spatial structure but phase shifted by β.

The Koopman eigenfunctions corresponding (4.26)–(4.28) are

$$|\phi_{1,0}| = \mu/r_0^2 - 1, \quad \arg(\phi_{1,0}) = 0, \tag{4.31a}$$

$$|\phi_{1,1}| = \mu/r_0^2 - 1, \quad \arg(\phi_{1,1}) = \theta_0 + \beta \ln\left(\frac{\sqrt{\mu}}{r_0}\right), \tag{4.31b}$$

$$|\phi_{1,2}| = \mu/r_0^2 - 1, \quad \arg(\phi_{1,2}) = 2\theta_0 + 2\beta \ln\left(\frac{\sqrt{\mu}}{r_0}\right). \tag{4.31c}$$

The magnitude of the Koopman eigenfunctions is zero at the limit cycle if the initial state is exactly on the limit cycle $r_0 = \sqrt{\mu}$. When $r_0 \neq \sqrt{\mu}$, the significance of the transient modes – in terms of their relative contribution to the flow trajectory $\boldsymbol{u}$ – strongly depends on the flow field at $t = 0$. As one may expect, the magnitudes grow with the distance of the initial amplitude from the limit cycle. Note that higher-order transient modes, $\boldsymbol{v}_{j,m}$ for $j = 2, 3, \ldots,$ decay faster both in time (with the exponent $j\sigma$) and in amplitude (as $(\mu/r_0^2 - 1)^j$) as j increases.

The physical significance and symmetry of the Koopman modes are summarized in table 1.

5. Dynamic mode decomposition

We show in this section that the DMD algorithm provides an approximation to the derived Koopman modes and eigenvalues. DMD is one method in the category of techniques of fitting a linear combination of exponential terms to a finite number of samples of a function spaced equally in time. In other words, we wish to model $\boldsymbol{u}(t)$ by a sum of $r + 1$ exponential terms,

$$\tilde{\boldsymbol{u}}(t) = \sum_{j=0}^{r} \tilde{\boldsymbol{v}}_j \exp(\tilde{\lambda}_j t). \tag{5.1}$$

Here, $\tilde{\boldsymbol{v}}_j \in \mathbb{C}^n$ is the Ritz vector corresponding to the Ritz value $\tilde{\lambda}_j \in \mathbb{C}$, with $\tilde{\lambda}_i \neq \tilde{\lambda}_j$ for $i \neq j$. The general objective is to identify r, the Ritz values and vectors such that $\tilde{\boldsymbol{u}}(t)$ is a least-squares fit to $\boldsymbol{u}(t)$. The connection between expansion into Ritz vectors and Koopman modes was made in Rowley *et al.* (2009). By comparing the expansions (5.1) and (2.2), we may expect $\tilde{\boldsymbol{v}}_j \approx \phi_j \boldsymbol{v}_j$ and $\tilde{\lambda}_j \approx \lambda_j$.

The DMD algorithm provides Ritz vectors (i.e. corresponding to dynamic modes in Schmid 2010) and values by an exact fit of the first r samples and a least-square fit of the last sample. The algorithm is not optimal (Chen *et al.* 2012) for finding the Ritz vector and values in (5.1) and may be sensitive to noise (Duke *et al.* 2012), but it is a direct method (as opposed to iterative) with a reasonably cheap computational cost. Suppose that we have sampled the flow $r+1$ times at a constant time interval Δt, i.e. $\boldsymbol{u}_0, \boldsymbol{u}_1, \ldots, \boldsymbol{u}_r$, where $\boldsymbol{u}_k = \boldsymbol{u}(\Delta t k)$. The Ritz values $\tilde{\lambda}_j$ and Ritz vectors $\tilde{\boldsymbol{v}}_j$ of this sequence satisfy

$$\boldsymbol{u}_k = \sum_{j=0}^{r-1} \tilde{\boldsymbol{v}}_j \exp(\tilde{\lambda}_j k \Delta t), \quad k = 0, 1, \ldots, r-1, \tag{5.2}$$

and

$$\boldsymbol{u}_r = \sum_{j=0}^{r-1} \tilde{\boldsymbol{v}}_j \exp(\tilde{\lambda}_j r \Delta t) + \boldsymbol{r} \quad \text{for } \boldsymbol{r} \perp \text{span}(\boldsymbol{u}_0, \boldsymbol{u}_1 \ldots, \boldsymbol{u}_{r-1}). \tag{5.3}$$

These discrete-time expansions are special case of (5.1).

5.1. *The algorithm*

The DMD algorithm in its simplest form consists of the following three steps.

(*a*) Write the $(r+1)$th sample $(\boldsymbol{u}_r)$ as linear combination of the first r states and an error term, i.e.

$$\boldsymbol{u}_r = c_0\boldsymbol{u}_0 + c_1\boldsymbol{u}_1 + \cdots + c_{r-1}\boldsymbol{u}_{r-1} + \boldsymbol{r} = \boldsymbol{X}\boldsymbol{c} + \boldsymbol{r}, \tag{5.4}$$

where $\boldsymbol{c} = [c_0, \ldots, c_{r-1}]^{\mathrm{T}}$, $\boldsymbol{X} = [\boldsymbol{u}_0, \boldsymbol{u}_1 \ldots, \boldsymbol{u}_{r-1}] \in \mathbb{R}^{n\times r}$ and $\boldsymbol{r} \perp \text{span}(\boldsymbol{X})$. Then solve the least-square problem for $\boldsymbol{c}$,

$$\boldsymbol{c} = \boldsymbol{X}^{+}\boldsymbol{u}_r, \tag{5.5}$$

where $\boldsymbol{X}^{+} = (\boldsymbol{X}^{*}\boldsymbol{X})^{-1}\boldsymbol{X}^{*}$ is the pseudo-inverse of $\boldsymbol{X}$.

(*b* Form a matrix in companion form,

$$\boldsymbol{C} = \begin{bmatrix} 0 & 0 & \ldots & 0 & c_0 \\ 1 & 0 & \ldots & 0 & c_1 \\ 0 & 1 & \ldots & 0 & c_2 \\ \vdots & & \ddots & & \vdots \\ 0 & 0 & \ldots & 1 & c_{r-1} \end{bmatrix} \in \mathbb{R}^{r\times r}, \tag{5.6}$$

and diagonalize it

$$\boldsymbol{C} = \boldsymbol{T}\boldsymbol{\Lambda}\boldsymbol{T}^{-1}. \tag{5.7}$$

(*c*) Finally, construct the matrix

$$\boldsymbol{V} = \boldsymbol{X}\boldsymbol{T}. \tag{5.8}$$

The Ritz values are then given by diagonal elements of $\boldsymbol{\Lambda}$ and the Ritz vectors by the columns of $\boldsymbol{V}$. Further details on the algorithm can be found in Rowley *et al.* (2009), Schmid (2010) and Chen *et al.* (2012).

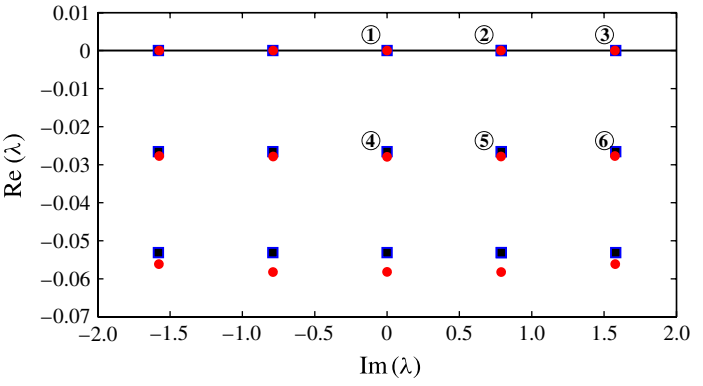

FIGURE 4. (Colour online) Koopman eigenvalues obtained from the formula (4.17) with values given in (5.9) are depicted with squares (blue online). Ritz values obtained from direct numerical simulation of the N–S equations at $Re = 50$ for $t \in [700–1400]$ are depicted with circles (red online). Ritz vectors associated with eigenvalues labelled ①–⑥ are shown in figures 5 and 6.

The residual of the DMD algorithm is small if the state at the final time is nearly linearly dependent on the previous states. This is certainly a reasonable assumption if a sufficiently long data sequence is collected from the periodic fully saturated flow. However, we can also expect the assumption to be good for transient trajectories approaching the limit cycle, as long as sufficiently many points on the limit cycle are included. The average residual levels out due to the fact that the columns of $\boldsymbol{X}$ become increasingly linearly dependent as they align with the most dominant Ritz vectors (Schmid 2010). The vector norms $s_j = \|\tilde{\boldsymbol{v}}_j\|$, often display a decay of several orders of magnitude for the first few Ritz vectors. The condition number of the Ritz vector j is $\kappa = s_j/s_0$ and provides a way to identify numerically sensitive modes. The threshold in the results presented in the following sections is $\kappa \in O(10^{-5}–10^{-6})$. Finally, we mention that one can improve the stability of the above algorithm via a similarity transformation of the companion matrix (Schmid 2010) based on the singular value decomposition (SVD) of $\boldsymbol{X}$. When using the SVD algorithm, the correct norm of the modes can be recovered from (5.2), as shown by Chen *et al.* (2012).

5.2. *Ritz vectors and values in intervals III–IV*

We collect snapshots from $t = 700$ to $t = 1400$ (with $\Delta t = 1$) from a direct numerical simulation (DNS) of the flow past a circular cylinder at $Re = 50$. During this time interval the state evolution is restricted to the local stable manifold of the limit cycle and to the limit cycle (intervals III–IV in figure 2).

In figure 4, the Ritz values $\tilde{\lambda}_{j,m}$ of this data set are compared to the Koopman eigenvalues given by (4.17). At $Re = 50$ the frequency and Lyapunov exponent of the limit cycle are approximately (see Sipp & Lebedev 2007)

$$\sigma = -2\epsilon\mu \approx -0.03, \tag{5.9a}$$

$$\omega = \omega_0 + \epsilon\omega_1 \approx 0.79. \tag{5.9b}$$

These values are thus the theoretical prediction of the horizontal and vertical spacing of the lattice formed by the Koopman eigenvalues. We observe that $\tilde{\lambda}_{j,m} \approx \lambda_{j,m}$, i.e. the Ritz values are collocated on this lattice.

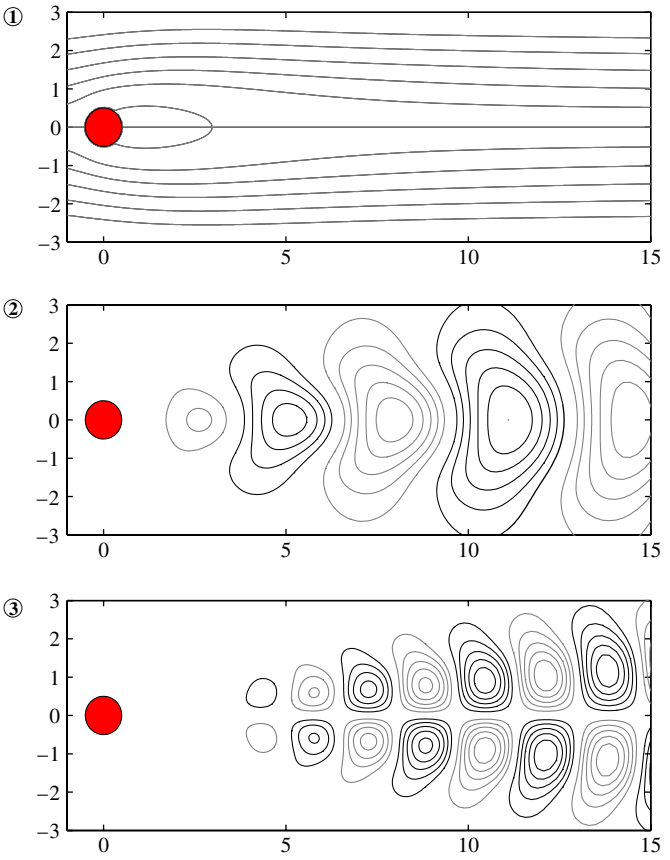

FIGURE 5. (Colour online) Ritz vectors corresponding to the attractor modes of the cylinder flow at $Re = 50$. Contours show the stream function, where positive (negative) values are depicted with black (grey) lines. Labels ①–③ correspond to the Ritz values in figure 4. The modes are complex and shown at one phase only.

The Ritz vectors associated with Ritz values in figure 4 are shown in figures 5 and 6. The DMD-extracted modes correspond to the Koopman modes listed in table 1. The three first Ritz vectors on the limit cycle ($j = 0, m = 0, 1, 2$) corresponding to the eigenvalues labelled ①–③ are shown in figure 5. The zeroth mode, $\tilde{\boldsymbol{v}}_{0,0}$ is the time-averaged flow on the limit cycle and has a reflection symmetry about the centreline $y = 0$. The first mode $\tilde{\boldsymbol{v}}_{0,1}$ corresponds to the part of the flow field that oscillates with the fundamental vortex shedding frequency ω_0. This mode has the same spatio-temporal symmetry and the same streamwise spacing between the vortices as the full nonlinear cylinder flow. The second mode $\tilde{\boldsymbol{v}}_{0,2}$ is due to the interaction of the first mode with itself. The second harmonic oscillates with twice the fundamental frequency and shows opposite symmetry to the first mode.

The Ritz vectors corresponding to transient Koopman modes ($j = 1, m = 0, 1, 2$) are shown in figure 6. As predicted by the analysis in the previous section, we observe that the transient fundamental (label ⑤) and second harmonic (⑥) modes have the same spatial structure as their corresponding asymptotic modes (② and ③); their difference is a matter of magnitude and phase. The shift mode (④) is a transient

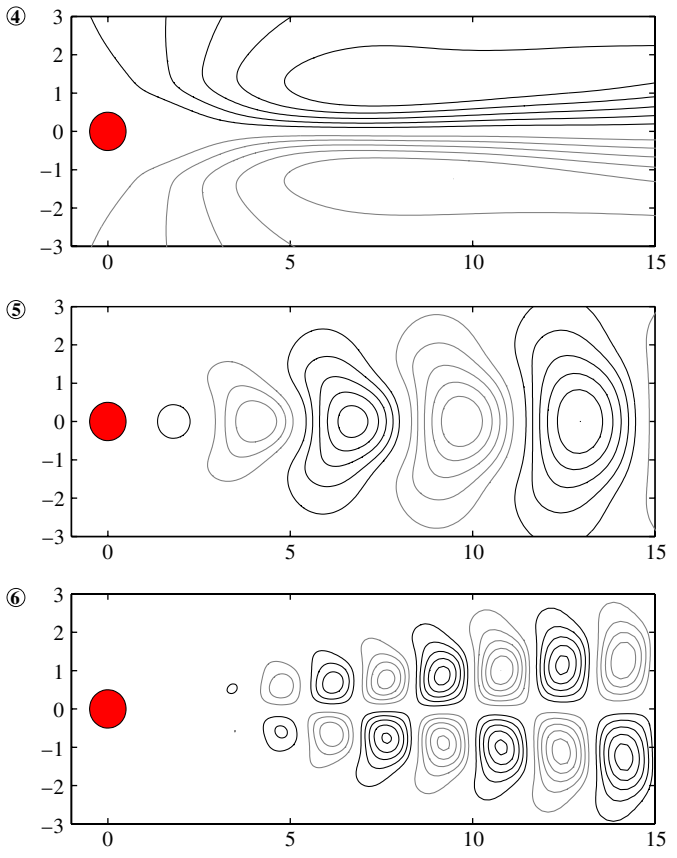

FIGURE 6. (Colour online) Ritz vectors corresponding to the transient modes of the cylinder flow at $Re = 50$. Contours show the stream function, where positive (negative) values are depicted with black (grey) lines. Labels ④–⑥ correspond to the Ritz values in figure 4. The modes are complex and shown at one phase only.

structure that has no resemblance to any asymptotic mode; it consists of the difference between the mean flow and the steady unstable equilibrium. This mode characterizes the decay of the recirculation zone when the flow departs from the steady solution to the time-averaged solution.

5.3. *Ritz values in intervals I–IV*

In figure 7, Ritz values of $\boldsymbol{X}$ containing snapshots from $t = 500$ to $t = 1400$ are shown. This sequence of data also includes samples from the early transient (intervals I–II in figure 2), where the state evolution initially is not near the limit cycle.

Despite the fact that $\boldsymbol{X}$ contains samples of exponentially growing structures within time interval I, all Ritz values are stable. Since the dynamics in $\boldsymbol{X}$ is globally stable (e.g. the state saturates on a limit cycle) a least-square fit of exponential terms cannot predict unbounded growth. We observe distinct discrete eigenvalues on the imaginary axis, in good agreement with the asymptotic ($j = 0$) Koopman eigenvalues in (4.17). The remaining Ritz values, however, are significantly different from those shown in figure 4 and do not correspond to any values predicted by (4.17). Instead they form distinct continuous branches for each frequency. In contrast to the asymptotic Ritz

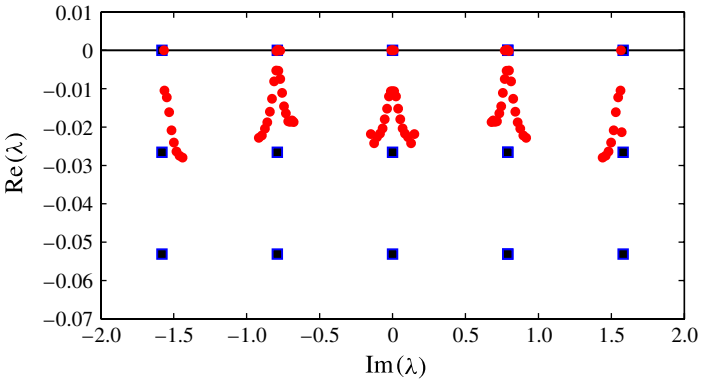

FIGURE 7. (Colour online) Ritz values obtained from Navier–Stokes equation at $Re = 50$ for $t \in [500–1400]$ are depicted with circles (red online), whereas the Koopman eigenvalues obtained from the formula (4.17) with values given in (5.9) are depicted with squares (blue online).

values, the complex branches are very sensitive to the choice of DMD parameters. In particular, the location of the branches in the vertical direction is sensitive to the amount of algebraic growth/decay in the transient trajectory, which makes this part of the spectrum highly dependent on the collected data set. As the algebraic growth increases, i.e. sampling closer to the unstable equilibrium point, the complex branch approaches the imaginary axis. The reason for the appearance of the complex branch is that DMD is attempting to describe the nonlinear data set with a linear combination of exponential terms. When the sampled data contains non-exponential behaviour, it needs a cluster of complex modes to describe the dynamics. We do not exclude the possibility that these transient Ritz values correspond to some other Koopman eigenvalues, for example a continuous set, than those derived in (4.17).

6. Koopman eigenvalues at $Re > Re_c$

In this section, we derive the Koopman eigenvalues of a limit cycle for any Reynolds number. Let $g(\boldsymbol{u})$ denote a scalar-valued bounded observable of the flow field. We define the Koopman operator with respect to the Navier–Stokes equations as

$$\frac{\partial g}{\partial t} = (\boldsymbol{f}(\boldsymbol{u}) \cdot \boldsymbol{\nabla}) g = Lg, \quad \rightarrow \quad U_t = \exp(Lt), \tag{6.1}$$

where $\boldsymbol{f}(\boldsymbol{u})$ satisfies

$$\frac{\partial \boldsymbol{u}}{\partial t} = \boldsymbol{f}(\boldsymbol{u}; Re), \tag{6.2}$$

and represents the spatially discretized Navier–Stokes equations of dimension $n = 2N_xN_y$. The integration (in our case using a second-order semi-implicit method) of (6.2) may formally be represented by a time-forward map, defined as

$$\boldsymbol{u}(s+t) = T_t(\boldsymbol{u}(s)). \tag{6.3}$$

Given a field at time s, T_t provides the field at a later time $t+s$ on the trajectory.

From relation (4.17), we have established an explicit expression for the Koopman eigenvalues in terms of the fundamental frequency and Lyapunov exponent of the limit

cycle for Re slightly larger than Re_c. As we show below, the trace formula developed in Gaspard (1998) and Cvitanović *et al.* (2013) establishes the relation (4.17) for $Re > Re_c$. In the following subsection, we determine the fundamental frequency (ω) and the Lyapunov exponent (σ) of a limit cycle using a Poincaré map. Then from the trace of the Koopman operator U_t

$$\mathrm{Tr}U_t = \sum_{j=0}^{\infty} \exp(\lambda_j t), \tag{6.4}$$

we analytically find an expression for the Koopman eigenvalues as a function of ω and σ.

6.1. *Linear stability*

The periodic flow may be described as a limit cycle solution to (6.3):

$$T_{rt_p}(\boldsymbol{u}_a) = \boldsymbol{u}_a, \quad r = 1, 2, \ldots, \tag{6.5}$$

where t_p is the period of oscillations. For stability analysis, it is convenient to describe the dynamics in an alternative discrete-time $t_k = k\Delta t$ setting using a Poincaré map. This map governs the dynamics on a hyper-surface $\mathscr{P}(\boldsymbol{u}) = 0$ in state-space, for which all pertinent trajectories intersect transversally. In other words, given a point $\boldsymbol{U}_k \in \mathbb{R}^{n-1}$ on the surface, the next point of intersection is given by the application of the Poincaré map S, i.e. $\boldsymbol{U}_{k+1} = S(\boldsymbol{U}_k)$. Applying S recursively, we may write the $(k+1)$th point as

$$\boldsymbol{U}_{k+1} = S^k \boldsymbol{U}_1, \tag{6.6}$$

where $\boldsymbol{U}_1$ is the initial point. A fixed point $\boldsymbol{U}_a$ of the Poincaré map satisfies

$$\boldsymbol{U}_a = S^{rk_p} \boldsymbol{U}_a, \quad r = 1, 2, \ldots, \tag{6.7}$$

and corresponds to a point on the limit cycle with the period $t_p = k_p \Delta t$. A Taylor expansion of S^{k_p} about $\boldsymbol{U}_a$ yields

$$S^{k_p}(\boldsymbol{U}_a + \delta\boldsymbol{U}) = \boldsymbol{U}_a + \boldsymbol{M}\delta\boldsymbol{U} + \cdots. \tag{6.8}$$

The monodromy matrix $\boldsymbol{M} = \nabla S^{k_p}(\boldsymbol{U}_a)$ of dimension $(n-1) \times (n-1)$ governs the dynamics of the small perturbation $\delta\boldsymbol{U}$. We order the eigenvalues of $\boldsymbol{M}$ (also known as Floquet multipliers) as

$$|\Lambda_1| \geqslant |\Lambda_2| \geqslant \cdots \geqslant |\Lambda_{n-1}|. \tag{6.9}$$

The limit cycle is stable if $|\Lambda_1| < 1$. The corresponding Floquet exponents are defined as

$$\mu_j = \frac{1}{t_p} \ln |\Lambda_j|. \tag{6.10}$$

The two most important characteristics of the limit cycle are thus the fundamental frequency and the Lyapunov exponent, defined by

$$\omega = \frac{2\pi}{t_p}, \quad \sigma = \mu_1 = \frac{1}{t_p} \ln |\Lambda_1|, \tag{6.11}$$

respectively.

6.2. *Trace formula for a limit cycle*

The general trace formula derived in Cvitanović & Eckhardt (1991), in the special case of a single limit cycle, is

$$\operatorname{Tr} U_t = t_p \sum_{r=1}^{\infty} \frac{\delta(t - rt_p)}{|\det(\boldsymbol{I} - \boldsymbol{M}^r)|}. \tag{6.12}$$

In appendix B we provide a brief derivation of this formula, following in particular Cvitanović (2013). The trace formula is a sum whose terms are non-zero only for integers of the limit cycle period. The rth non-zero term describes how much, after the rth return to the Poincaré section, a small neighbourhood volume (i.e. a tube) of the limit cycle has retracted. This relation thus connects the trace of U_t to the dynamics in the local stable manifold of the limit cycle.

In fact, from the Laplace transform of the above formula, one can identify the Koopman eigenvalues explicitly from the roots of a so-called Zeta function. The Laplace transform of the trace of U_t,

$$\int_0^{\infty} \mathrm{e}^{-st} \operatorname{Tr} U_t \, \mathrm{d}t = \operatorname{Tr} \frac{1}{s - L}, \tag{6.13}$$

indicates that the Koopman eigenvalues are the poles of the resolvent of L. By inserting (6.12) in the left-hand side of the above equation one obtains

$$\operatorname{Tr} \frac{1}{s - L} = \frac{\partial}{\partial s} \ln(Z(s)), \tag{6.14}$$

where $Z(s)$ is the so-called Zeta function (called the spectral determinant in Cvitanović *et al.* 2013),

$$Z(s) = \exp\left[-\sum_{r=1}^{\infty} \frac{1}{r} \frac{\mathrm{e}^{-stpr}}{|\det(\boldsymbol{I} - \boldsymbol{M}^r)|} \right]. \tag{6.15}$$

Now, since the determinant does not depend on the basis which $\boldsymbol{M}$ is described in, we may write it in terms of the eigenvalues of $\boldsymbol{M}$

$$\frac{1}{|\det(\boldsymbol{I} - \boldsymbol{M}^r)|} = \prod_{k=1}^{n-1} \frac{1}{1 - \Lambda_k^r}, \tag{6.16}$$

where we have assumed that $|\Lambda_k| < 1$ for all k. Note that the Taylor series of the two-dimensional function $(1 - x)^{-1}(1 - y)^{-1}$ is

$$(1 - x)^{-1}(1 - y)^{-1} = 1 + x + y + x^2 + xy + y^2 + \cdots, \tag{6.17}$$

when $|x| < 1$, $|y| < 1$. Each term in the product sequence (6.16) may thus be written as an infinite sum. Define a multi-index vector $\boldsymbol{j} = [j_1, j_2, \ldots, j_{n-1}]$ with elements as positive integers, $j_k = 0, 1, 2, \ldots$. Using the multi-index notation defined in appendix C, we may write (6.16) as

$$\frac{1}{|\det(\boldsymbol{I} - \boldsymbol{M}^r)|} = \sum_{\boldsymbol{j}} \boldsymbol{\Lambda}^{r\boldsymbol{j}} \tag{6.18}$$

and consequently the Zeta function as

$$Z(s) = \exp\left[-\sum_{r=1}^{\infty}\frac{1}{r}\left(\mathrm{e}^{-stp}\sum_{j}\boldsymbol{\Lambda}^{\boldsymbol{j}}\right)^{r}\right]. \tag{6.19}$$

Finally, applying the identity $\sum x^r/r = -\ln(1-x)$, we obtain the final form of the Zeta function for a limit cycle:

$$Z(s) = \prod_{\boldsymbol{j}}^{\infty}(1-\mathrm{e}^{-stp}\boldsymbol{\Lambda}^{\boldsymbol{j}}). \tag{6.20}$$

The zeros $Z(s) = 0$ are given by the zeros of individual terms in the product, i.e.

$$\exp[-t_p(s-\boldsymbol{\mu}\cdot\boldsymbol{j})] = 1. \tag{6.21}$$

Taking the logarithm of both sides, we obtain

$$s_{\boldsymbol{j},m} = \boldsymbol{\mu}\cdot\boldsymbol{j} + \mathrm{i}m\omega \tag{6.22}$$

with $m = 0, \pm1, \pm2, \ldots$. For our particular choice of analytic observables the spectrum of U_t is reduced to its minimal components, namely as any integer multiple of the stability eigenvalues.

6.3. *Koopman eigenvalues for the cylinder flow*

Consider the cylinder flow at $Re_{c,3D} > Re > Re_c$, where $Re_{c,3D} = 182$ is the critical Reynolds number for which the limit cycle becomes unstable. Suppose that the frequency and the Lyapunov exponent of the limit cycle are ω and σ respectively. Then, the Koopman eigenvalues $\lambda_{j_1,0,\ldots,0,m}$ obtained from (6.22) corresponding to this stability eigenvalue are

$$\lambda_{j,m} = j\sigma + \mathrm{i}m\omega, \tag{6.23}$$

with $j = 0, 1, 2\ldots$ and $m = 0, \pm1, \pm2, \ldots$. This formula agrees with the Koopman eigenvalues (4.17) derived in § 4 from a weakly nonlinear theory. Thus, for any stable limit cycle, the Koopman eigenvalues form a lattice on the lower half of the complex plane. The marginal eigenvalues on the horizontal imaginary axis corresponding to $j = 0$ correspond to the non-decaying time-averaged mean ($m = 0$) and periodic dynamics ($m \neq 0$) on the limit cycle. The remaining eigenvalues $j \neq 0$ are decaying and describe the transient behaviour of flow in the local stable manifold of the limit cycle.

7. Discussion

We have limited the analysis to a periodic orbit and to observables that are bounded and smooth, where only a discrete spectrum exists. The Koopman eigenvalues (6.23) associated with the limit cycle are only a subset of the discrete spectrum of U_t. If significant transients are considered, then the unstable equilibrium also contributes to the flow dynamics and consequently to the spectrum of U_t. In fact, the full Koopman spectrum (for analytical observables) consists of the union of the eigenvalues associated with the two critical elements (Gaspard 1998). For chaotic attractors and/or by enlarging the functional space of observables, eigenvalues other than those given by the trace formula may be found. In fact, the non-periodic part of the attractor has a continuous spectrum, resulting in an additional term in the expansion of an observable in the form of an integral. Mezić (2005) showed that the decomposition of

a chaotic attractor into a mean, periodic and fluctuating part is a rigorous version of the 'triple decomposition' for turbulent flows (Reynolds & Hussain 1972). Moreover, the fluctuating part of the field is more conveniently treated as a stochastic process, for which the POD modes are the appropriate expansion basis. Thus, when Koopman modes were introduced by Mezić (2005), they were considered as a complement to POD modes and not a replacement.

It has been argued that Koopman modes are a nonlinear generalization of linear global stability modes. In fact, it was shown in Rowley *et al.* (2009) that for a linear flow $\boldsymbol{f}(\boldsymbol{u}) = \boldsymbol{A}\boldsymbol{u}$, the Koopman modes are equivalent to linear global modes and the Koopman eigenvalues are equivalent to stability eigenvalues. This result holds even if $\boldsymbol{A}$ is unstable, and hence also if the solutions are unbounded. The relationship between linear stability analysis and Koopman modes for bounded observables is however very different. If an unstable equilibrium co-exists with an attractor which naturally results in bounded observables, then all Koopman eigenvalues are stable. The characterization of unstable dynamics is more appropriately done with the adjoint Koopman operator, which is the well-known Perron–Frobenuis operator (Cvitanović *et al.* 2013). There is an analogy between the adjoint-direct Koopman operator and the adjoint-direct linear Navier–Stokes operator for convection-dominated open shear flows. These flows are characterized by convective non-normality (Marquet *et al.* 2009): the linear stability eigenmodes are located far downstream where the response to upstream incoming disturbances is large; the corresponding adjoint global modes on the other hand are located upstream, characterizing the sensitivity of the flow to disturbances. Similarly. the Koopman modes are located near or on an attractor, whereas the corresponding adjoint modes are located 'upstream' in time, near the unstable dynamics.

8. Conclusions

In this paper, we have explicitly constructed Koopman modes for flows developing and undergoing self-sustained oscillations by using a standard multiple-scale expansion of the flow field in combination with a spectral expansion of the amplitude. The spatial structures describe the asymptotic dynamics on the limit cycle and the transient dynamics on the local stable manifold of the limit cycle. They correspond to the time-averaged mean flow, the shift mode and nonlinear fundamental/higher-harmonic global modes. The frequencies and growth rates of the modes form a lattice in the lower-half of the complex plane, where the spacing in the vertical and horizontal directions correspond, respectively, to the fundamental frequency and the Lyapunov exponent of the oscillator. This is in accordance with the formulae derived by forming the trace of the Koopman operator.

We have established a relationship between the Koopman modes and the Ritz vectors obtained from the dynamic mode decomposition algorithm. We showed that near and on the attractor, the Ritz vectors and values of an appropriate empirical data set approximate Koopman modes and eigenvalues. When the sampled dynamics is far from the limit cycle, where the influence of unstable basic flow may be significant, the Ritz values corresponding to transient Ritz vectors cluster together and do not correspond to any of the derived discrete Koopman eigenvalues. Whether these Ritz values correspond to Koopman eigenvalues other than those predicted by the trace formula remains to be investigated.

Since its introduction by Schmid (2010), DMD is becoming an increasingly popular post-processing tool, in fluid-dynamical applications particularly, but also in other applied areas. The algorithm allows, in a rather straightforward manner, the

extraction of physical (or 'dynamic') information from huge data sets generated from experimental devices or large-scale numerical simulations. The approximation of Koopman modes is only one application of the algorithm; when viewed as curve-fit of sampled data, it can also be useful to approximate linear eigenvalue problems (Schmid 2010), discrete Fourier transforms (Chen *et al.* 2012), etc. This particular work together with Rowley *et al.* (2009) puts the DMD algorithm on a firm mathematical base within the field of evolution operators for the particular class of flows with intrinsic periodic behaviour. However, further validation between Ritz values and Koopman modes for chaotic and noisy systems, pertaining for example to high-Reynolds-number flows, remains to be conducted. It seems, however, that the standard DMD algorithm is sensitive to noise-contaminated data (Duke *et al.* 2012). For the application of DMD to more complicated configurations a promising, albeit more expensive, variant of the algorithm is the 'Optimized' DMD introduced by Chen *et al.* (2012).

Acknowledgements

The author is grateful to I. Mezić, P. Schmid and P. Cvitanović for many interesting discussions. This work was supported by the Swedish Research Council (VR-2010-3910).

Appendix A. Derivation of equations (4.11)–(4.14)

The Koopman eigenfunctions, eigenvalues and expansion coefficients are derived with respect to the S–L equation (see also Gaspard *et al.* 1995; Gaspard & Tasaki 2001). The observable $g(A)$ in polar coordinates is a periodic function in θ and may thus be represented as

$$g(A) = \sum_{m=-\infty}^{\infty} \hat{g}_m(r) \exp(\mathrm{i}m\theta). \tag{A 1}$$

Inserting (4.2*b*) in the exponent of (A 1), we obtain

$$\begin{aligned} g(A) &= \sum_{m=-\infty}^{\infty} \hat{g}_m(r) \exp\left[\mathrm{i}m(\theta_0 + \omega_1\tau + \beta \ln\left(\frac{r}{r_0}\right)\right] \\ &= \sum_{m=-\infty}^{\infty} \left[\hat{g}_m(r)\left(\frac{r}{r_0}\right)^{\mathrm{i}m\beta}\right] \exp\left[\mathrm{i}m(\theta_0 + \omega_1\tau)\right]. \end{aligned} \tag{A 2}$$

To put the above expression in the form of (4.9), we need to extract the exponential decay rate $\mathrm{e}^{-2\mu\tau}$ from the terms in the brackets of (A 2). Rewrite $r(\tau)$ as a function of the new variable y,

$$r(\tau) = \sqrt{\frac{\mu}{1 + y(\tau)}}, \tag{A 3}$$

with

$$y(\tau) = \frac{\mu}{r(\tau)^2} - 1 = \left(\frac{\mu}{r_0^2} - 1\right) \exp(-2\mu\tau), \tag{A 4}$$

where (4.2*a*) has been used. In the transformed variable we have

$$\hat{g}_m(r)\left(\frac{r}{r_0}\right)^{\mathrm{i}m\beta} = \left[\hat{g}_m\left(\sqrt{\frac{\mu}{1+y}}\right)(1+y)^{-\mathrm{i}m\beta/2}\right]\left(\frac{\sqrt{\mu}}{r_0}\right)^{\mathrm{i}m\beta}. \tag{A 5}$$

In the y-coordinate, the limit cycle at $r=\sqrt{\mu}$ is mapped to the origin $y=0$ and the repelling point at $r=0$ is mapped to infinity. This mapping is convenient if we are interested in the nonlinear attracting dynamics of the limit cycle at $y=0$ (i.e. intervals III and IV in figure 2). We thus Taylor expand (A 5) around $y=0$,

$$\hat{g}_m(r)\left(\frac{r}{r_0}\right)^{\mathrm{i}m\beta} = \sum_{j=0}^{\infty}\left\{\frac{1}{j!}\frac{\partial^{(j)}}{\partial y}\left[\hat{g}_m\left(\sqrt{\frac{\mu}{1+y}}\right)(1+y)^{-\mathrm{i}m\beta/2}\right]\right\}_{y=0}\left(\frac{\sqrt{\mu}}{r_0}\right)^{\mathrm{i}m\beta} y^j. \tag{A 6}$$

Denoting the complex scalar in the braces by $\alpha_{j,m}^{(g)}$ and transforming back from y to r_0, we have

$$\hat{g}_m(r)\left(\frac{r}{r_0}\right)^{\mathrm{i}m\beta} = \sum_{j=0}^{\infty}\alpha_{j,m}^{(g)}\left(\frac{\sqrt{\mu}}{r_0}\right)^{\mathrm{i}m\beta}\left(\frac{\mu}{r_0^2}-1\right)^j \exp(-2j\mu\tau). \tag{A 7}$$

By inserting the Taylor expansion into (A 2) we get the final spectral form of the observable,

$$\begin{aligned} g(A) &= \sum_{j=0}^{\infty}\sum_{m=-\infty}^{\infty}\alpha_{j,m}^{(g)}\left(\frac{\mu}{r_0^2}-1\right)^j \exp\left[\mathrm{i}m\left(\theta_0+\beta\ln\left(\frac{\sqrt{\mu}}{r_0}\right)\right)\right]\exp\left[(-2\mu j+\mathrm{i}m\omega_1)\tau\right] \\ &= \sum_{j=0}^{\infty}\sum_{m=-\infty}^{\infty}\alpha_{j,m}^{(g)}\phi_{j,m}\mathrm{e}^{\hat{\lambda}_{j,m}\tau}, \end{aligned} \tag{A 8}$$

and may identify the scalar expansion coefficients, the Koopman eigenfunctions and the Koopman eigenvalues. In a straightforward manner it can be verified that $\phi_{j,m}$ and $\hat{\lambda}_{j,m}$ satisfy (4.7) for $j=0,1,\ldots$ and $m=0,\pm1,\pm2,\ldots$.

Appendix B. Derivation of equation (6.12)

This appendix follows the derivations presented in Cvitanović (2013) and Gaspard (1998), except that the analysis is restricted to the simpler case of a limit cycle. The formal definition of a trace (6.4) assumes that we already have computed the eigenvalues of U_t. A different way of defining the trace of an evolution operator is in terms of its kernel. Using a Dirac-delta function, the Koopman operator for any bounded observable function $g(\boldsymbol{u})$ can be written as

$$U_t g(\boldsymbol{u}) = \int_{\mathscr{M}} \delta\left(\boldsymbol{w}-T_t(\boldsymbol{u})\right) g(\boldsymbol{w})\,\mathrm{d}\boldsymbol{w} \tag{B 1}$$

where $\boldsymbol{u}$ belongs to the manifold $\mathscr{M}\subset\mathbb{R}^n$. This form of the Koopman operator is similar to the form of integral operators, for which one may define the trace as

$$\mathrm{Tr}\mathscr{K} = \int_{\mathscr{M}} \mathscr{K}(\boldsymbol{u},\boldsymbol{u})\,\mathrm{d}\boldsymbol{u}, \tag{B 2}$$

where $\mathscr{K}$ is the kernel. Integral operators are in L^2-space as well as compact, that is they can in many respects be treated as finite-rank matrices. The kernel of U_t is singular and the operator is certainly not in L^2. However, if the dynamical system $\boldsymbol{f}$ is

real-analytic, it has an analytic continuation to a complex extension of the state space, where the singularity can be 'removed' and the problem reduced to the standard theory of integral operators (Artuso *et al.* 2013).

Inspired by this definition, we define the trace of the Koopman operator as

$$\operatorname{Tr} U_t = \int_{\mathscr{M}} \delta(\boldsymbol{u} - T_t(\boldsymbol{u}))\,\mathrm{d}\boldsymbol{u}. \tag{B 3}$$

From (B 3), one observes that the trace of U_t receives a contribution whenever the trajectory returns to the starting point after r repetitions of the limit cycle period t_p. Note that the trace is a property of the operator and independent of the observable. From (B 3), it is clear that the trace of U_t is only non-zero if $\boldsymbol{u} = T_t\boldsymbol{u}$. These trajectories are precisely those on the limit cycle or the equilibrium.

To proceed, we decompose the time-forward map T_t into two parts: the $(n–1)$-dimensional Poincaré map S and a one-dimensional return-time function τ. The Poincaré map captures the transverse part of the periodic dynamics, since the flow component tangent to the limit cycle, which is not in the span of the Poincaré surface, has not be taken into account. Assuming that the longitudinal state component has a certain mean velocity v as it traverses the limit cycle, one may transform this component to a time-coordinate system using the relation $v\,\mathrm{d}t$. Thus the full dynamics is described by the Poincaré map S and by the first-return function $\tau(\boldsymbol{U})$ that provides the (non-constant) time interval between successive points $\boldsymbol{U}$ on the Poincaré surface, e.g. $t_{k+1} = t_k + \tau(\boldsymbol{U}_k)$.

Applying τ recursively, we may write $(k+1)$th time as a function of the first point,

$$t_{k+1} = t_1 + \sum_{j=0}^{k-1} \tau(S^j\boldsymbol{U}_1). \tag{B 4}$$

Now, decompose the kernel of U_t (B 3) into two parts

$$\operatorname{Tr} U_t = \int_{\mathscr{P}(\boldsymbol{u})=0} \mathrm{d}\boldsymbol{U} \int_0^{\tau(\boldsymbol{U})} \mathrm{d}t\,\delta(\boldsymbol{U} - S^k\boldsymbol{U})\,\delta\left(t - \sum_{j=0}^{k-1} \tau(S^j\boldsymbol{U})\right), \tag{B 5}$$

where S^k and τ are defined in (6.6) and (B 4), respectively. We treat the two Dirac-delta functions separately, starting with S^k. First recall that the Dirac-delta function applied to a scalar-valued function $g(x)$ is

$$\int \delta(g(x))\,\mathrm{d}x = \int \delta(x)|g'(0)^{-1}|\,\mathrm{d}u = \sum_j \frac{1}{|g'(x_j)|}, \tag{B 6}$$

where x_j are the roots of $g(x)$. This property may be generalized to $n-1$ dimensions and applied to the first Dirac-delta in (B 5),

$$\int_{\mathscr{P}(\boldsymbol{u})=0} \delta(\boldsymbol{U} - S^k(\boldsymbol{U}))\,\mathrm{d}\boldsymbol{U} = \frac{1}{|\det(\boldsymbol{I} - \boldsymbol{M}^r)|}, \tag{B 7}$$

where $\boldsymbol{I}$ denotes the identity matrix. The second part of the trace can be written as (Cvitanović 2013)

$$\int_0^{\tau(\boldsymbol{U})} \delta\left(t - \sum_{j=0}^{k-1} \tau(S^j\boldsymbol{U})\right) \mathrm{d}t = t_p \sum_{r=1}^{\infty} \delta(t - rt_p). \tag{B 8}$$

Inserting the identities (B 7) and (B 8) in (B 5), we get the trace formula for a single limit cycle,

$$\operatorname{Tr} U_t = t_p \sum_{r=1}^{\infty} \frac{\delta(t - rT_p)}{|\det(\boldsymbol{I} - \boldsymbol{M}^r)|}, \tag{B 9}$$

which was first derived by Cvitanović & Eckhardt (1991).

Appendix C. Multi-index notation

Define a *multi-index* as an array of n non-negative integers $j_k = 0, 1, 2, \ldots$:

$$\boldsymbol{j} = [j_1, j_2, \ldots, j_n] \in \mathbb{N}^n, \tag{C 1}$$

Consider next the product of $n-1$ Floquet multipliers

$$\boldsymbol{\Lambda} = \Lambda_1 \Lambda_2 \cdots \Lambda_{n-1} = \exp[t_p(\mu_1 + \mu_2 + \cdots + \mu_{n-1})] \tag{C 2}$$

(the imaginary parts of complex pairs cancel in the exponent), and define

$$\boldsymbol{\mu} = [\mu_1, \mu_2, \ldots, \mu_{n-1}] \in \mathbb{R}^{n-1}. \tag{C 3}$$

Λ can now be raised to $\boldsymbol{j}$th power as

$$\boldsymbol{\Lambda}^{\boldsymbol{j}} = \exp(t_p \boldsymbol{\mu} \cdot \boldsymbol{j}) = \Lambda_1^{j_1} \Lambda_2^{j_2} \cdots \Lambda_{n-1}^{j_{n-1}}. \tag{C 4}$$

REFERENCES

ARTUSO, R., HUGH, R. & CVITANOVIĆ, P. 2013 'Why does it work?' In *Chaos: Classical and Quantum* (ed. P. Cvitanović, R. Artuso, R. Mainieri, G. Tanner & G. Vattay). Niels Bohr Institute, chaosBook.org/version14.

BARKLEY, D. 2006 Linear analysis of the cylinder wake mean flow. *Europhys. Lett.* **75**, 750–756.

CHEN, K., TU, J. H. & ROWLEY, C. W. 2012 Variants of dynamic mode decomposition: boundary condition, Koopman, and Fourier analyses. *J. Nonlinear Sci.* **22** (6), 887–915.

CHOMAZ, J. M. 2005 Global instabilities in spatially developing flows: non-normality and nonlinearity. *Annu. Rev. Fluid Mech.* **37**, 357–392.

CVITANOVIĆ, P. 2013 'Trace formulas'. In *Chaos: Classical and Quantum* (ed. P. Cvitanović, R. Artuso, R. Mainieri, G. Tanner & G. Vattay). Niels Bohr Institute, chaosBook.org/version14.

CVITANOVIĆ, P., ARTUSO, R., MAINIERI, R., TANNER, G. & VATTAY, G. (Eds) 2013 *Chaos: Classical and Quantum*. Niels Bohr Institute, chaosBook.org.

CVITANOVIĆ, P. & ECKHARDT, B. 1991 Periodic orbit expansions for classical smooth flows. *J. Phys.* A: *Math. Gen.* **24**, L237–L241.

DUKE, D., SORIA, J. & HONNERY, D. 2012 An error analysis of the dynamic mode decomposition. *Exp. Fluids* **52**, 529–542.

GASPARD, P. 1998 *Chaos, Scattering, and Statistical Mechanics*. Cambridge University Press.

GASPARD, P., NICOLIS, G., PROVATA, A. & TASAKI, S. 1995 Spectral signature of the pitchfork bifurcation: Liouville equation approach. *Phys. Rev.* E **51** (1), 74–94.

GASPARD, P. & TASAKI, S. 2001 Liouvillian dynamics of the Hopf bifurcation. *Phys. Rev.* E **64**, 056232.

GUCKENHEIMER, J. & HOLMES, P. 1983 *Nonlinear Oscillations, Dynamical System and Bifuracations of Vector Fields*. Springer.

HUERRE, P. & MONKEWITZ, P. 1990 Local and global instabilities in spatially developing flows. *Annu. Rev. Fluid Mech.* **22**, 473–537.

KOOPMAN, B. 1931 Hamiltonian systems and transformations in Hilbert space. *Proc. Natl Acad. Sci. USA* **17**, 315–318.

LASOTA, A. & MACKEY, C. M. 1994 *Chaos, Fractals and Noise: Stochastic Aspects of Dynamics*. Springer.

LUMLEY, J. L. 1970 *Stochastic Tools in Turbulence*. Academic.

MARQUET, O., LOMBARDI, M., CHOMAZ, J. M., SIPP, D. & JACQUIN, L. 2009 Direct and adjoint global modes of a recirculation bubble: lift-up and convective non-normalities. *J. Fluid Mech.* **622**, 1–21.

MEZIĆ, I. 2005 Spectral properties of dynamical systems, model reduction and decompositions. *Nonlinear Dyn.* **41** (1), 309–325.

MEZIĆ, I. 2013 Analysis of fluid flows via spectral properties of the koopman operator. *Annu. Rev. Fluid Mech.* **45** (1), 357–378.

MULD, T., EFRAIMSSON, G. & HENNINGSON, D. 2012 Mode decomposition on surface-mounted cube. *Flow Turbul. Combust.* **88**, 279–310.

NOACK, B., AFANASIEV, K., MORZYNSKI, M., TADMOR, G. & THIELE, F. 2003 A hierarchy of low-dimensional models for the transient and post-transient cylinder wake. *J. Fluid Mech.* **497**, 335–363.

PEROT, J. B. 1993 An analysis of the fractional step method. *J. Comput. Phys.* **108** (1), 51–58.

PIER, B. 2002 On the frequency selection of finite-amplitude vortex shedding in the cylinder wake. *J. Fluid Mech.* **458**, 407–417.

PROVANSAL, M., MATHIS, C. & BOYER, L. 1987 Bénard–von Kármán instability: transient and forcing regimes. *J. Fluid Mech.* **182**, 1–22.

REYNOLDS, W. C. & HUSSAIN, A. K. M. F. 1972 The mechanics of an organized wave in turbulent shear flow. Part 3. Theoretical models and comparisons with experiments. *J. Fluid Mech.* **54** (2), 263–288.

ROWLEY, C. W., MEZIĆ, I., BAGHERI, S., SCHLATTER, P. & HENNINGSON, D. S. 2009 Spectral analysis of nonlinear flows. *J. Fluid Mech.* **641**, 115–127.

SCHMID, P. J. 2007 Nonmodal stability theory. *Annu. Rev. Fluid Mech.* **39**, 129–162.

SCHMID, P. J. 2010 Dynamic mode decomposition of numerical and experimental data. *J. Fluid Mech.* **656**, 5–28.

SCHMID, P. 2011 Application of the dynamic mode decomposition to experimental data. *Exp. Fluids* **50**, 1123–1130.

SCHMID, P., LI, L., JUNIPER, M. & PUST, O. 2011 Applications of the dynamic mode decomposition. *Theoret. Comput. Fluid Dyn.* **25**, 249–259.

SEENA, A. & SUNG, H. J. 2011 Dynamic mode decomposition of turbulent cavity flows for self-sustained oscillations. *Intl J. Heat Fluid Flow* **32** (6), 1098–1110.

SEMERARO, O., BELLANI, G. & LUNDELL, F. 2012 Analysis of time-resolved piv measurements of a confined turbulent jet using pod and Koopman modes. *Exp. Fluids*, **53** (5), 1203–1220.

SIPP, D. & LEBEDEV, A. 2007 Global stability of base and mean flows: a general approach and its applications to cylinder and open cavity flows. *J. Fluid Mech.* **593**, 333–358.

TADMOR, G., LEHMANN, O., NOACK, B. & MORZYNSKI, M. 2010 Mean field representation of the natural and actuated cylinder wake flow. *Phys. Fluids* **22**, 034102.

TAIRA, K. & COLONIUS, T. 2007 The immersed boundary method: a projection approach. *J. Comput. Phys.* **225**, 2118–2137.

THIRIA, B. & WESFREID, J. E. 2007 Stability properties of forced wakes. *J. Fluid Mech.* **579**, 137–161.